The Thesis Committee for Andrew Charles Johnson
Certifies that this is the approved version of the following thesis:

Investigations of Porous Media using Nuclear Magnetic Resonance Secular Relaxation Measurements and Micro-CT Image Analysis

APPROVED BY
SUPERVISING COMMITTEE:

Supervisor:

Hugh C. Daigle

Carlos Torres-Verdin

Investigations of Porous Media using Nuclear Magnetic Resonance Secular Relaxation Measurements and Micro-CT Image Analysis

by

Andrew Charles Johnson, B.S.

Thesis

Presented to the Faculty of the Graduate School of

The University of Texas at Austin

in Partial Fulfillment

of the Requirements

for the Degree of

Master of Science in Engineering

The University of Texas at Austin

August 2015

Acknowledgements

I would like to express my sincerest gratitude to my adviser, Dr. Hugh Daigle, for his tireless attention, guidance, and knowledge. As a teacher, adviser, and mentor, he has made my time at the University of Texas both a challenging and greatly rewarding experience.

Dr. Maša Prodanović's exciting and enlightening image analysis course was the foundation for the image anlaysis component of this project. Dr. Prodanović was also very generous with her time, providing many hours of one-on-one assistance with 3D medial axis software and general image analysis guidance.

I would also like to thank Dr. Carlos Torres-Verdin for his expert technical advice and for taking a genuine interest in my project. His help was essential to quality delivery of the final product.

A great thank you to David Medellin for his generous personal attention and technical assistance using his simultaneous NMR inversion code, particularly when I needed it most.

And finally, I would like to thank my lab mates, Han Jiang, Chunxiao Zhu, and Sanjay Surya, for being so accommodating and flexible despite their busy research schedules.

Abstract

Investigations of Porous Media using Nuclear Magnetic Resonance Secular Relaxation Measurements and Micro-CT Image Analysis

Andrew Charles Johnson, M.S.E.

The University of Texas at Austin, 2015

Supervisor: Hugh C. Daigle

Nuclear magnetic resonance (NMR) has been used as a common and powerful tool for petrophysical investigation of fluid-bearing porous media. A common application in this field is the extraction of pore size distributions, which are important descriptors of pore system morphologies. The common technique is to correlate mercury-injection porosimetry (MICP) measurements with NMR T_1 or T_2 distributions to obtain NMR-derived pore sizes. The limitations of MICP include pore-throat sensitivity and percolation effects, which compromise interpretation of results. Micro-CT image analysis has no such limitations, and measurements of pore size are characterized by pore body voxel counts. Presented are image analysis and NMR-correlated results for samples of Berea sandstone and Silurian dolomite. These results are compared to MICP-correlated results and the discrepancies interpreted as pore throat-to-body aspect ratios.

Nuclear magnetic resonance pore size distributions are valid for single-phase fluids in the fast-diffusion NMR relaxation regime. When the effects of proton diffusion through internal magnetic field gradients become prominent, however, this relationship becomes entangled. Simultaneous measurement of longitudinal (T_1) and transverse (T_2) relaxation times using combined inversion recovery-CPMG pulse sequences allows for interpretation of a computed NMR attribute called secular relaxation (T_{2sec}). This quantity is defined as the difference in transverse and longitudinal relaxation rates ($1/T_2$-$1/T_1$) and can reveal important pore system properties. Presented are results that extract internal magnetic field gradient strengths based on changes in T_{2sec} as a function of the NMR experimental parameter τ. Further results consider a two-dimensional χ^2 analysis to attempt to invert for mean pore size and the difference in transverse and longitudinal surface relaxivities. The benefit of these types of analyses is to provide a simple methodology for inferring the average strengths of internal magnetic field gradients and pore sizes from NMR measurements without the need for independent measurements of pore size distributions, such as from mercury injection porosimetry. In addition, secular relaxation analysis removes the effects of bulk fluid relaxation.

Table of Contents

List of Figures

Chapter 1: Introduction

Nuclear Magnetic Resonance (NMR) describes the behavior of nuclear magnetic moments in the presence of applied magnetic fields. The discovery of this phenomenon in 1946 led to the development of powerful empirical techniques spanning a wide range of scientific and engineering disciplines, including medicine, chemistry, materials science, and others. Among these applications, studies of NMR measurements performed on fluid-saturated sedimentary rocks have proven extraordinarily useful to the oil and gas industry. The success of this technique can be attributed to the quick, economic, and powerful nature of NMR logging, which at present can yield key fluid-flow properties of a reservoir, including permeability, porosity, and fluid saturations for a wide range of rock types and characteristics. As NMR continues to advance in an increasingly technology-driven industry, its use as a premier well logging and petrophysical analysis tool, particularly for unconventional reservoirs, becomes increasingly viable. Studies like the one offered in this thesis will be required to fully understand and utilize the power of NMR in a progressive oil and gas industry. Presented are empirical results and new analytical approaches to interpreting NMR data. The hope is that these findings will aid in the eventual discovery of novel and practical NMR logging techniques capable of rapidly extracting new petrophysical information from complex oil and gas reservoirs.

1.1 Research Objectives and Motivation

This project includes both experimental and modeling components. Nuclear magnetic resonance behavior in conventional sedimentary rocks was explored using primary NMR measurements as well as computed attributes from advanced measurements. These experimental findings were then compared with theoretical models.

Empirical methods entailed NMR T_1, T_2, and simultaneous T_1 and T_2 measurements, mercury injection porosimetry measurements, and micro-CT images. Analysis of NMR responses included the fast-diffusion regime formulation of NMR pore size distributions correlated with experimental pore-size measurements and image analysis results. Modeling and prediction of NMR responses were performed for samples of Berea sandstone, Boise sandstone, Silurian dolomite, and a 0.25 mm bead pack. A diffusion model for an idealized pore geometry was used to extract pore system information for these samples. The objectives of this project were to:

(1) Investigate micro-CT image analysis as a correlation method for NMR measurements in the determination of NMR surface relaxivity and pore size distributions. Compare results with the standard MICP method and interpret incongruities.

(2) Interpret trends in an NMR computed value called secular relaxation through the lens of a restricted diffusion model as a function of the NMR inter-echo half-spacing parameter τ.

(3) Show that variation in secular relaxation measurements can be quantified as a function of τ and yield information about volumetrically weighted average internal magnetic field gradients.

(4) Consider surface relaxation in parallel with a restricted diffusion model in the context of secular relaxation measurements to invert for pore size and surface relaxivities.

1.2 NUCLEAR MAGNETIC RESONANCE THEORY AND BACKGROUND

1.2.1 Basic NMR Physics

This section will seek to explain the phenomenon of nuclear magnetic resonance from basic physics principles. Since hydrogen nuclei (H^+) resonances are most typically observed in porous media experiments, the fundamentals of proton NMR are presented here. Physics dictates that protons have the quantum mechanical property of spin, possessing values of either spin $m = ½$ or $m = -½$. This spin quantity gives the proton an intrinsic magnetic moment, which causes the proton to behave as a tiny magnetic dipole (see Figure 1.1, left panel). Normally, the spin states $m = ½$ and $m = -½$ are energetically degenerate, which means that the energy of the proton is the same regardless of its spin. However, a famous physics experiment, called the "Stern-Gerlach" experiment, first showed that when a static magnetic field $\mathbf{B_0}$ is applied, the proton takes on one of two discrete quantized energy states, depending on its spin value. If the proton has spin $m = ½$, it aligns with the magnetic field and resides in the low-energy state; if it has spin $m = -½$, it aligns against the magnetic field and resides in the high-energy state (Figure 1.1, right panel).

The energy of a magnetic dipole in a magnetic field $\mathbf{B_0}$ is given by

$$E = -\boldsymbol{\mu} \cdot \boldsymbol{B_0} = -\gamma m \hbar B_0$$

for protons, where γ is the gyromagnetic ratio, a constant for an H^+ nucleus. Therefore, the low energy state is $E(m = ½) = -\gamma\hbar B_0/2$ and the high energy state is $E(m = -½) = \gamma\hbar B_0/2$. The difference in the two energy levels is then equal to $\Delta E = \gamma\hbar B_0$ (see Figure 1.2). An electromagnetic wave with energy equal to $\Delta E = \gamma\hbar B_0 = h\nu$ can be easily absorbed by the system in the form of a transition from the $m = ½$ to the $m = -½$

state. Solving for the frequency corresponding to such an absorption gives $\nu = \gamma B_0/2\pi$. This frequency has been given the name Larmor frequency and is the frequency for which resonant absorption is observed. A system of protons irradiated with RF waves with frequency equal to the Larmor frequency may incite phase transitions of protons in the $m = ½$ state to the $m = -½$ state, which can be observed in a measurement of radiofrequency power absorption. This is the so-named "stationary" or "continuous-wave (CW)" NMR measurement method, which most clearly elucidates the NMR phenomenon. In the following section, some more common albeit more complex experiments – T_1 and T_2 relaxation times using a dynamic or "pulsed" NMR method – are introduced.

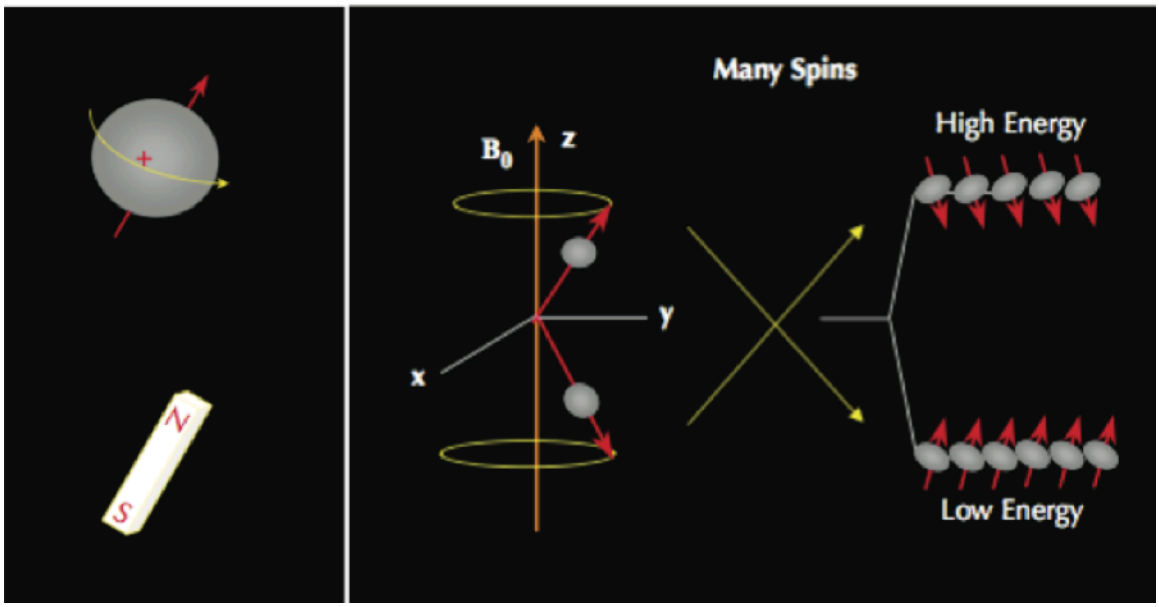

Figure 1.1 (from Coates, 1999): Left panel – The spin of a proton generates a small magnetic moment, represented in the figure by a red arrow. The moment causes the proton to act as a magnetic dipole. Right panel – In the presence of an applied magnetic field $\mathbf{B_0}$, the dipole can exist in one of two energy states; it can either precess along the direction of the field (low energy) or along a vector opposite the field (high energy).

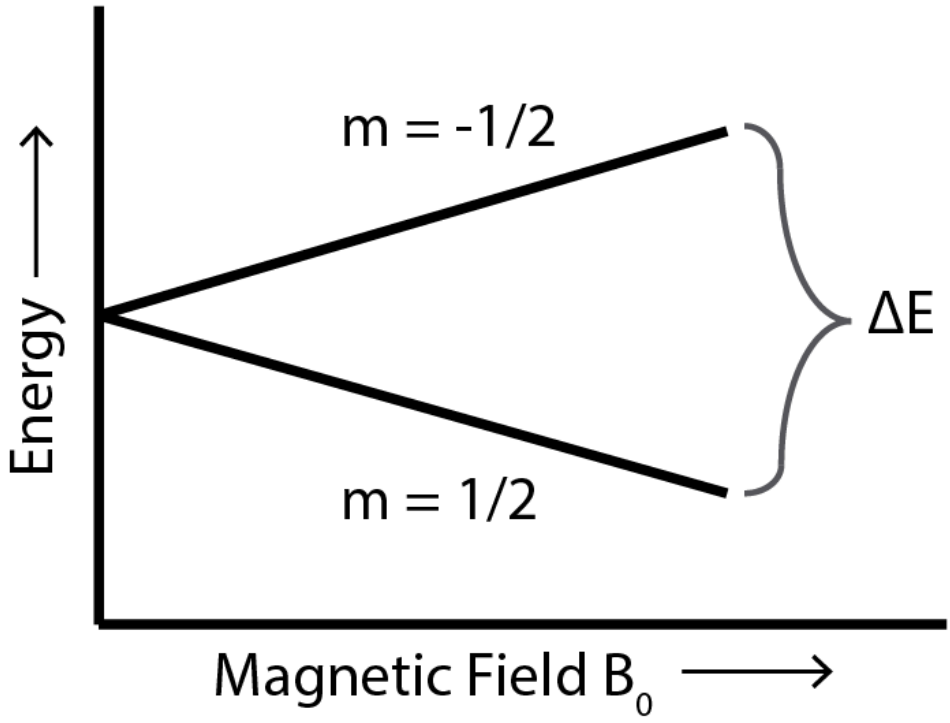

Figure 1.2: Proton spin states $m = ½$ and $m = -½$ are energetically degenerate when no magnetic field is present. An energy differential arises when a non-zero magnetic field $\mathbf{B_0}$ is applied. The magnitude of the energy difference is proportional to the applied field strength.

1.2.2 The NMR experiment: T_1 and T_2 Measurements

Consider the experimental setup shown in Figure 1.3. A fluid or fluid-saturated sample (e.g. water-saturated sandstone) is placed in a tube inside a large magnet, a radiofrequency (RF) source, and a detector coil. The large magnet produces a large static magnetic field $\mathbf{B_0}$, while the radiofrequency source produces a secondary time varying magnetic field $\mathbf{B_1}$. The detector coil is provided to detect small changes in the net magnetization of the sample in response to the applied fields $\mathbf{B_0}$ and $\mathbf{B_1}$.

A typical NMR experiment consists of two primary measurements. The first, the longitudinal, or "spin-lattice" relaxation time (T_1), is a measure of the time necessary for proton magnetic moments to align with $\mathbf{B_0}$. The second measurement, transverse, or "spin-spin" relaxation time (T_2), is a measure of precession decoherence as proton spins

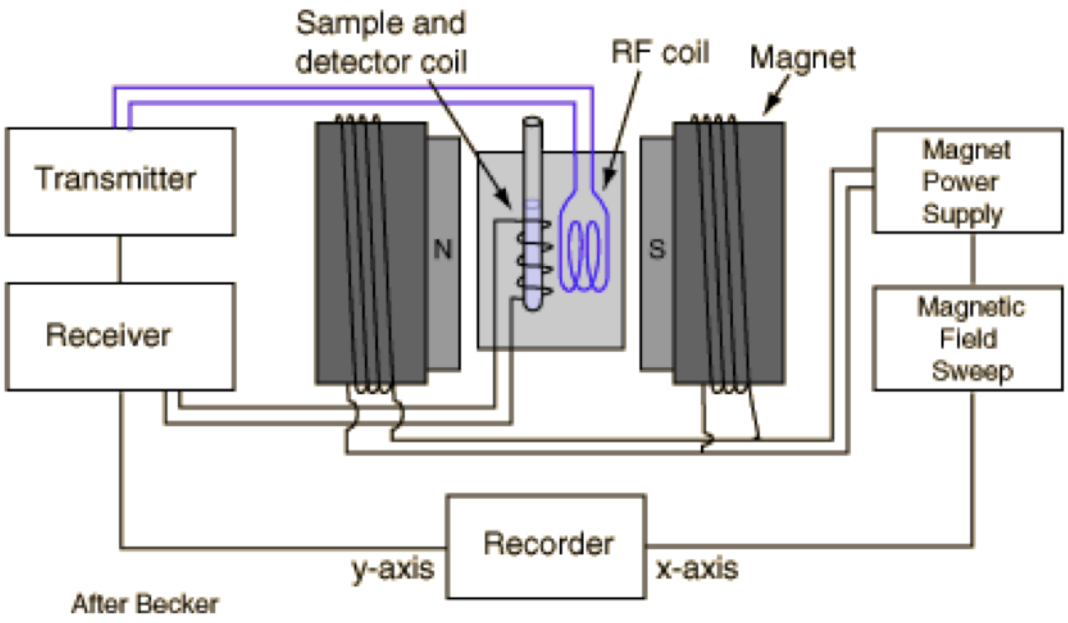

Figure 1.3 (from Nave, 2012): A simplified NMR experiment layout. The sample is placed in a tube inside a large magnet that produces a primary static magnetic field. A radiofrequency source produces pulses of RF waves. Changes in the net magnetization response of the sample are detected using a copper detector coil.

interact with one another and diffuse in the presence of $\mathbf{B_1}$ and $\mathbf{B_0}$.

To better understand the course of these measurements, consider the following. Since proton moments will preferentially align with $\mathbf{B_0}$, a preponderance of magnetic moments in the low energy state will develop. This contributes to a net magnetization of the system in the longitudinal direction parallel to $\mathbf{B_0}$ once equilibrium is achieved. The timescale associated with the development of equilibrated magnetization is governed by

$$M(t) = M_0(1 - e^{-\frac{t}{T_1}})$$

where T_1 corresponds to the time constant of magnetization, called the "longitudinal relaxation time," and where M_0 represents the equilibrium net magnetization of the system. This expression is for a system with initially zero net magnetization and may vary by an exponential prefactor if magnetization is initially nonzero (i.e. inverted). Longitudinal relaxation is often also called "spin-lattice" relaxation to indicate the physical means by which relaxation occurs; spins thermally transfer energy with surroundings (the "lattice") whereby dropping to lower energy states to contribute to macroscopic magnetic equilibrium. The preceding T_1 experiment is called "saturation recovery." Often, however, net initial magnetization is first inverted using polarized radiofrequency pulses so that the net magnetization vector lies antiparallel to M_0. In such a T_1 experiment, called "inversion recovery," magnetization evolution is described by

$$M(t) = M_0(1 - 2e^{-\frac{t}{T_1}})$$

This is the more common way of measuring T_1 relaxation, and the method employed in this project.

Measurement of transverse relaxation (T_2) is slightly more complex than a T_1 experiment. First note that proton magnetic moments in either of the two possible energy states do not perfectly align with the applied field, but instead precess about field lines at a precise frequency, called the Larmor frequency. For protons, this frequency is directly proportional to the strength of the applied field. Considering a system of protons that is in equilibrium with a static field $\mathbf{B_0}$, as at the end of the previously described T_1 experiment, RF waves tuned to the Larmor frequency may then be irradiated on the system. This is typically done in discrete pulses of RF energy. The first pulse of Larmor RF waves has the effect of causing precession of the various spins to cycle in phase with one another. Equivalently, the presence of this electromagnetic field pulse briefly homogenizes the Larmor frequencies of protons throughout the system. As spins then precess about $\mathbf{B_0}$ field lines in unison, the net macroscopic magnetization itself precesses about the applied magnetic field. The precessing component of this magnetization is detectable in the transverse plane. As radiation is absorbed in spin-state transitions, the longitudinal component of the magnetization vector decreases, and by the end of the RF pulse, the net magnetization vector exists only in the transverse plane. The first RF pulse is called the 90° pulse—its name indicating the rotation of the net magnetization vector from alignment with the applied field into the perpendicular transverse plane (Figure 1.4a). As soon as this pulse ends, spins rapidly dephase, and the magnitude of transverse magnetization exponentially decays. This "free induction decay" (T_2*) occurs on a timescale several orders of magnitude faster than T_1, so that longitudinal magnetization remains very close to zero during the process. Once transverse magnetization has fully decayed, spin coherence can yet be revived with the use of another RF pulse –called a 180° pulse – which has the effect of reversing the directions of individual spins (or more strictly speaking, changing their phases by 180°) such that they subsequently and

momentarily rephase. Rephasing occurs because a 180° phase change effectively puts slower-phased spins ahead (in phase space) of faster-phased spins, so that faster spins will then "catch up" to slower spins (Figures 1.4b, 1.4c). This transient rephasing creates a brief macroscopic magnetization in the transverse plane, called a "spin echo." The spins again dephase, and another 180° pulse is instated, whereby another brief rephasing spin echo occurs. This pulse-echo-pulse-echo process is repeated many times, and the amplitudes of the magnetic echoes are recorded in the receiver coil at each rephasing. An important feature of this experiment is that the 180° pulses are not completely efficient at rephasing proton spins at each interval. Phase coherence is lost whenever protons feel different local magnetic field strengths and thus precess with different Larmor frequencies. Dephasing due to these field heterogeneities is reversible with a 180° RF pulse if those heterogeneities remain constant with time, as do heterogeneities in $\mathbf{B_0}$. Irreversible losses, however, occur due to random processes, including interactions between proton spins and with unpaired electrons, or as spins diffuse and move through other magnetic field heterogeneities. Irreversible dephasing gives rise to a net observed reduction in the amplitude of the spin echo after each RF pulse (Figure 1.5). The rate of decay of these amplitudes is characterized by the time constant T_2.

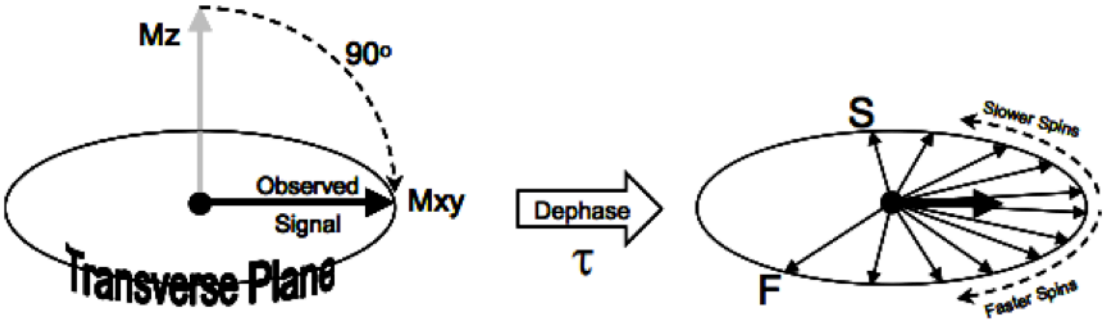

Figure 1.4a (from Alley and Korosec, 2009): As Larmour-frequency RF waves are irradiated on the system (90° pulse), spins precess in unison and create a net magnetization that precesses in the transverse plane. At the same time, energy is absorbed by the system until longitudinal magnetization (Mz) is fully diminished and magnetization lies only in the transverse plane. Once the RF source is shutoff, spins dephase due to magnetic field heterogeneities.

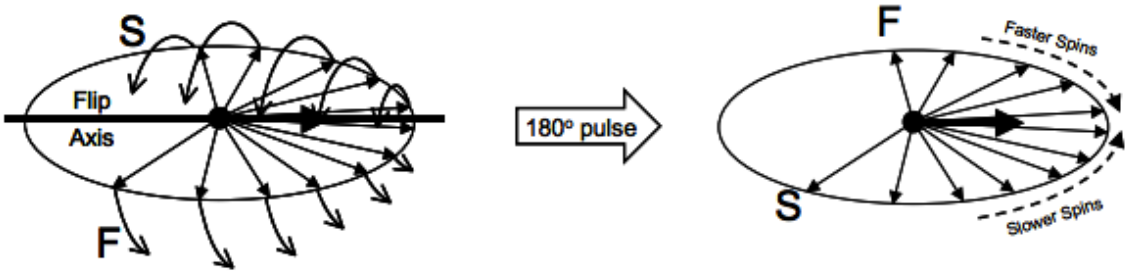

Figure 1.4b: An 180° RF pulse is applied after phases lose coherence. The pulse effectively flips spins so that faster spins are placed before slower spins in phase space, causing them to effectively "catch up" to slower spins.

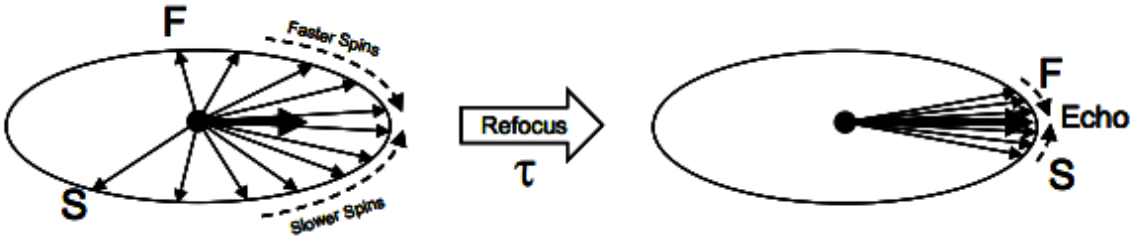

Figure 1.4c: After the 180° pulse, phase reversal allows spins to briefly rephase, so that a large population of phases momentarily align. This manifests as a transient magnetization detectable in the transverse plane, called a spin echo.

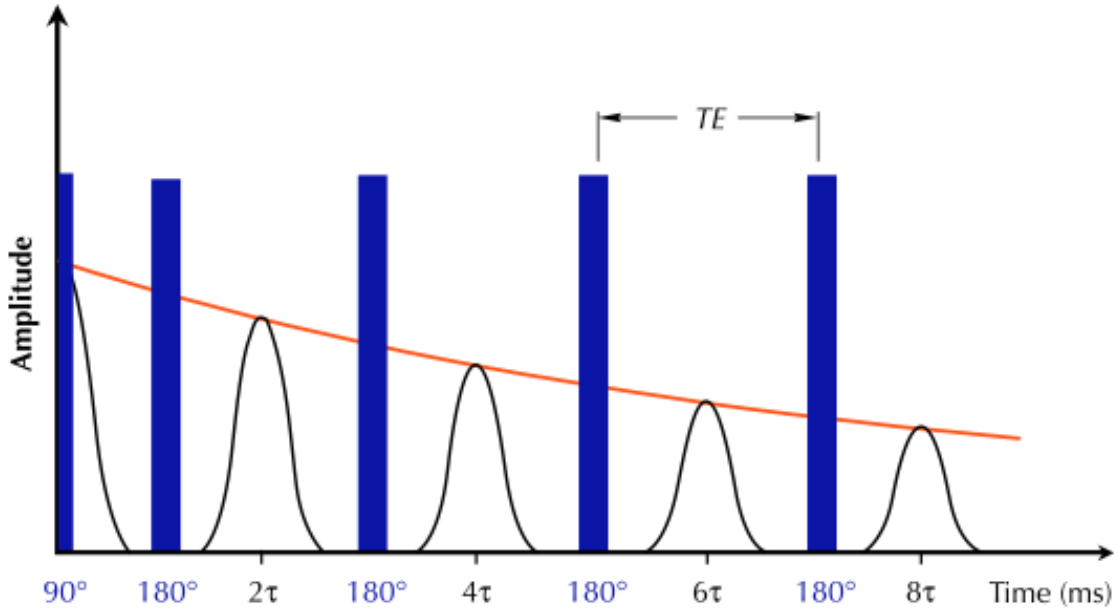

Figure 1.5 (from Coates, 1999): An echo decay train that characterizes the transverse relaxation parameter T_2. Radiofrequency pulses (90° and 180°) are represented by the blue bars. Decay in the amplitudes of spin echoes due to irreversible dephasing is shown by the red curve. Decay time is characterized by the parameter T_2.

1.2.3 Applications to Porous Media

This section summarizes the concepts relevant to NMR analysis of porous media. For a fuller development and history of the concepts presented here, see Section 2.

The application of NMR to porous media commonly makes use of the finding that both longitudinal and transverse relaxation processes occur predominantly at the contact boundaries of pore fluids and pore walls. Assuming that diffusion of fluid molecules occurs rapidly enough that protons traverse a pore several times before relaxing ("fast diffusion," **S2.1**), the transverse and longitudinal relaxation rates are proportional to pore surface-to-volume ratios:

$$\frac{1}{T_1} = \rho_1 \left(\frac{S}{V}\right)_{pore}$$

$$\frac{1}{T_2} = \rho_2 \left(\frac{S}{V}\right)_{pore}$$

where the constants of proportionality $\rho_1$and ρ_2 represent the strength of relaxation at pore walls and are typically determined for a particular mineralogy using an independent empirical measurement (**S2.1**). These expressions then define a straightforward relationship between pore size and relaxation time. A pore system with a distribution of pore sizes will be reflected as a distribution of T_1 or T_2 values, shifted by the surface relaxivity values ρ_1 and ρ_2 respectively.

1.2.4 Restricted Diffusion Relaxation

The fast-diffusion analysis for NMR relaxation in porous media holds true when internal magnetic field gradients are constant and diffusion of proton spins through field heterogeneities is negligible compared to the measurement timescale. In many rocks, however, and particularly those containing magnetic species, these assumptions lose traction. Three classes of processes contribute to relaxation. They include bulk fluid, surface, and diffusion relaxation processes – the effects of which add in parallel (**S2.1**):

$$\frac{1}{T_1} = \frac{1}{T_{1B}} + \frac{1}{T_{1S}}$$

$$\frac{1}{T_2} = \frac{1}{T_{2B}} + \frac{1}{T_{2S}} + \frac{1}{T_{2D}}$$

If diffusion of protons in pore fluids occurs such that spins move through magnetic field heterogeneities, but not so fast that these heterogeneities are motionally averaged over the scale of the pore (fast-diffusion), rephasing by each 180° RF pulse will be ineffective and additional relaxation, $T_{2D,}$ will occur. Note that T_{2D} is strictly a transverse relaxation phenomenon. Bulk (T_{1B}, T_{2B}) and surface (T_{1S}, T_{2S}) relaxation mechanisms affect both T_1 and T_2 relaxation, although not necessarily by the same molecular processes (Kleinberg, 1999).

Modern NMR equipment allows for special pulse sequences with the ability to measure T_1 and T_2 relaxation times simultaneously. This type of measurement reveals fluid volumes correlated with particular T_1-T_2 combinations and allows for extraction of additional pore system information. Secular relaxation time has been defined as the difference in transverse and longitudinal relaxation times:

$$\frac{1}{T_{2sec}} = \frac{1}{T_2} - \frac{1}{T_1} = \frac{1}{T_{2S}} - \frac{1}{T_{1S}} + \frac{1}{T_{2D}}$$

assuming that $T_{1B} = T_{2B}$, which is the case for most fluids. In the expression for T_{2sec}, the only term that depends on the echo half-spacing parameter τ is T_{2D}. Therefore any observed change in the T_{2sec} response as a consequence of varying τ can be modeled using T_{2D} variation alone.

Expressions developed for surface relaxation as a function of pore surface-to-volume ratio and surface relaxivity (Brownstein and Tarr, 1979), and diffusion relaxation as a function of internal magnetic field gradient, fluid self-diffusion coefficient, and pulse sequence echo spacing (Neuman, 1974), make secular relaxation experiments and modeling useful in characterizing key pore system parameters.

$$\frac{1}{T_{2S}} = \rho_2 \left(\frac{S}{V}\right)_{pore}$$

$$\frac{1}{T_{1S}} = \rho_1 \left(\frac{S}{V}\right)_{pore}$$

T_{2D} behavior has been characterized analytically for a single spherical pore:

$$\frac{1}{T_{2D}} = -\frac{2\gamma^2 G R^4}{D} \sum_{i=1}^{\infty} \left[\frac{1}{\alpha_i^4(\alpha_i^2 - 2)} \left(1 - \frac{3 - 4\exp\left(-\frac{\tau\alpha_i{}^2 D}{R^2}\right) + \exp\left(-\frac{2\tau\alpha_i{}^2 D}{R^2}\right)}{\frac{2\tau\alpha_i{}^2 D}{R^2}} \right) \right]$$

where R is the radius of the pore, γ is the gyromagnetic ratio for protons, G is the average internal magnetic field gradient strength, and D is the fluid self diffusion coefficient. The values α_i are given by the roots of $\tan(\alpha_i) = 2\alpha_i/(2-\alpha_i^2)$.

The secular relaxation response may be modeled using the formulation above. This approach provides a potential simultaneous inversion for pore size, internal gradient, and surface relaxivities. Parameters of the system that are known from independent measurements may be included in the model to better ascertain the unknowns.

Chapter 2: Literature Review

2.1 Conventional NMR Analyses

In Section **S1.2.3**, a simple relationship between relaxation time and pore size was presented. It described a direct proportionality of a pore's surface-to-volume ratio to its inverse relaxation time, or equivalently suggested that an NMR relaxation spectrum could be interpreted as a pore size distribution. This idea has been demonstrated experimentally (Straley et al., 1991) by showing that centrifugation of water out of increasingly smaller pores in a rock corresponded to a loss of signal at increasingly smaller NMR relaxation times. However, theoretical development of this relationship began much earlier with the modeling of catalyzed relaxation rates at pore boundaries (Bloch, 1951; Brown and Fatt, 1956). The work of Korringa et al. (1959, 1962), considered these "wall effects" of relaxation due to interactions of proton spins with paramagnetic ions at pore-grain boundaries. A spherical pore was considered with paramagnetic sites distributed evenly at the pore surface. Microwaves were introduced at the resonant frequency of the paramagnetic sites, and through a process called the Overhauser effect (Erb et al., 1958), transferred energy to spins in a thin layer near the surface. This created spin-state transitions to higher energy states. It was shown that, by assuming that the timescale of diffusion of protons between pore boundaries was much faster than relaxation within the bulk fluid, the polarization of the system was both uniform and independent of pore shape. This defined a "fast-diffusion" regime that would later be applied in relaxation theory.

Brownstein and Tarr (1979) furthered the work of Korringa et al. by mathematically considering a system of diffusing proton spins in the presence of relaxation sinks of idealized geometries. Starting with the diffusion equation for a

volume-like sink, a boundary condition for a surface-like sink, and an initial condition stating uniform initial magnetization, the magnetization density tensor was derived and shown to be described by an eigenvalue problem. Protons were said to diffuse with diffusivity tensor D (proportional to rate of diffusion of proton spins within the system), in the presence of a relaxation sink of strength M (i.e., pore boundary paramagnetic relaxation strength), and an active surface S (i.e. surface area of pore boundary). A result of this formulation, given the assumption that $Ma/D << 1$, was that the decay time at the surface sink could be represented simply as $T_0 = V/MS$, where the subscript 0 reflected the finding that the lowest eigenmode dominated the solution. Though spherical, cylindrical, and planar geometries were considered, functional dependence of decay times was found to be similar throughout. The stipulation that $Ma/D << 1$ defined a "fast-diffusion" regime, valid for fast diffusion compared to the combined effect of relaxation strength M and the distance between relaxation centers a. This relationship is modernly expressed as

$$\frac{1}{T_{1,2S}} = \rho_{1,2}\left(\frac{S}{V}\right)_{pore}$$

where the surface relaxivity ρ is an empirical parameter typically dependent on grain mineralogy and experimental method.

Relaxation processes have been generally categorized into three genres, which include bulk relaxation processes, surface relaxation mechanisms, and relaxation due to diffusion. The classification of these processes began when Hahn (1950) first noted that shifts in local magnetic fields could not be accounted for by diamagnetic relaxation mechanisms alone, and cited a study by Ramsey (1950) that showed that field shifts

could be explained by molecule-specific paramagnetism. In porous media, diamagnetic relaxation occurs in bulk fluids, while paramagnetic relaxation occurs at pore-grain boundaries, which define the first two classes of relaxation mechanisms. The third relaxation effect was qualitatively noted by Hahn and was understood to be due to phase coherence loss as proton spins diffused through magnetic field heterogeneities. This effect was quantitatively analyzed by Carr and Purcell (1954) by developing a special RF pulse-sequence that improved upon the Hahn decay echo succession. Prior to this work, measurement of an echo decay envelope had to be done with multiple overlain 90°-180° pulse sequence measurements (see Figure 2.1). Carr and Purcell designed a 90°-180°-180°-180°… pulse sequence that could effectively reduce phase dispersion (or equivalently, the effect of relaxation due to diffusion) as a function of the number of 180° echoes. Using a random walk analysis, they showed mathematically that phase dispersion as a function of time using Hahn's method was given by

$$< \phi_D >_{AVE} = 2G^2\gamma^2 D t^3/3$$

where G represents the average internal field gradient strength, γ represents the proton gyromagnetic ratio, and D represents the fluid diffusion coefficient. The analysis was then repeated for the multiple-180° pulse method, incorporating the effect of each pulse to reverse the sign of terms in the phase dispersion expression. The result was an original phase dispersion reduced by a factor of $1/n^2$, where n is the number of 180° pulses:

$$< \phi_D >_{AVE} = 2G^2\gamma^2 D t^3/3n^2$$

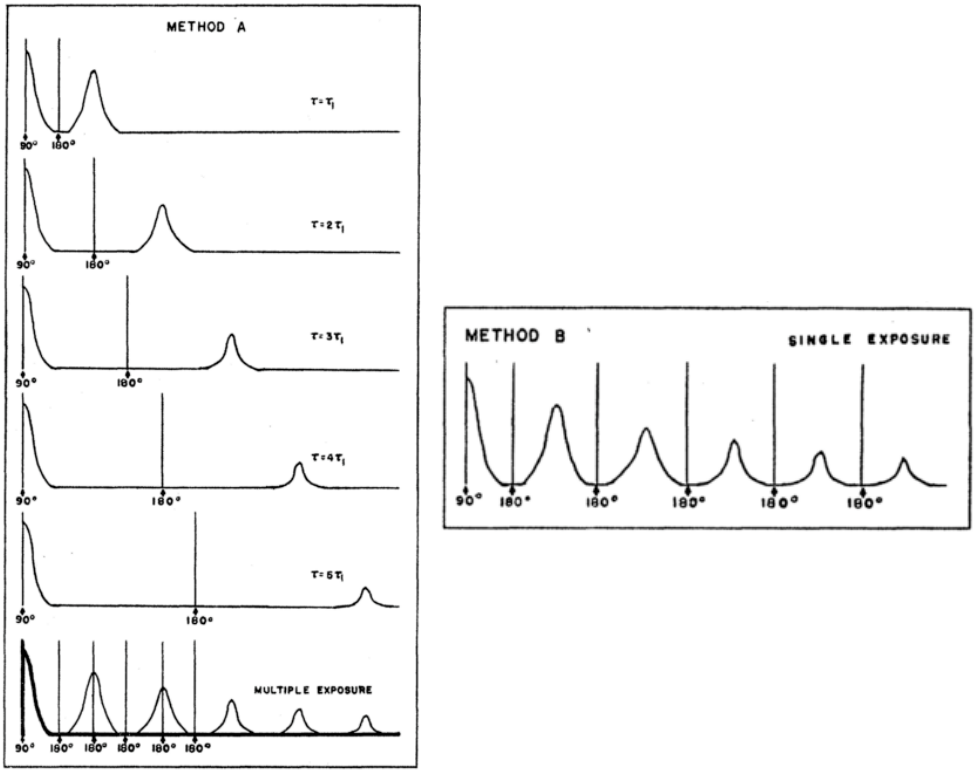

Figure 2.1 (from Carr and Purcell, 1954): The left panel (Method A) is the original method which required several separate 90°-180° pulse experiments which were then superposed to determine net decay time. The right panel (Method B) represents the Carr-Purcell method of a 90° pulse followed by a sequence of equally spaced 180° pulses. Method B has the advantage of toggling the spacing between echoes and reducing the effect of diffusion relaxation in the decay envelope.

The total magnetization of the system was then shown to be

$$M(t) = M_0 exp\left[\left(-\frac{t}{T_2}\right) + \left(-\frac{\gamma^2 G^2 D t^3}{12n^2}\right)\right]$$

where T_2 is called the "natural" (non-diffusional) relaxation and the second term represents additional relaxation due to diffusion:

$$\frac{1}{T_{2D}} = \frac{\gamma^2 G^2 D\, TE^2}{12}$$

where *TE* is the spacing between each 180° pulse. Note that diffusion relaxation appears exclusively a transverse relaxation effect, since phase coherence and loss thereof occurs in the transverse plane.

Combining the results from these three processes can be done by summing them in parallel (ex. Dunn et al., 1994; Kleinberg, 1999; Coates et al. 1991):

$$\frac{1}{T_1} = \frac{1}{T_{1B}} + \frac{1}{T_{1S}} = \frac{1}{T_{1B}} + \rho_1 \left(\frac{S}{V}\right)_{pore}$$

$$\frac{1}{T_2} = \frac{1}{T_{2B}} + \frac{1}{T_{2S}} + \frac{1}{T_{2D}} = \frac{1}{T_{2B}} + \rho_2 \left(\frac{S}{V}\right)_{pore} + \frac{\gamma^2 G^2 D\, TE^2}{12}$$

which are equivalent to the expressions presented in Chapter 1.

Kleinberg and Horsfield pointed out the limitations of expressing diffusion relaxation in the above form when diffusing molecules encountered impenetrable boundaries in a porous medium. Treatments of this limitation have been considered

(e.g. Wayne and Cotts, 1966; Robertson, 1966; Tarczon and Halperin, 1985), one of which quantitatively modeled relaxation due to diffusion in idealized pore geometries as a function of pore size, internal magnetic field gradient, and CPMG inter-echo spacing ($TE = 2\tau$) (Neuman, 1974). Neuman's formulation considered the probability distribution P of magnetic moment phase shifts – a measure of coherence in proton precession and therefore transverse relaxation – as Gaussian:

$$P(\phi, 2\tau) = (2\pi(\phi^2))^{-1/2}\exp\left[-\frac{\phi^2}{2 < \phi^2 >}\right]$$

For the case of non-restricted diffusion, the net resulting magnetic moment as a function of time as was computed as (Carr and Purcell, 1954):

$$M(2\tau) = M_0 \int_{-\infty}^{\infty} P(\phi, 2\tau)\, cos\phi\, d\phi$$

where M_0 is the net magnetic moment in the absence of a field gradient. The assumption of Gaussian-distributed phase shifts was shown to remain valid for short echo spacing compared to the time necessary for proton diffusion between boundaries. Neuman noted that phase distribution need not be normal for all geometries, but concluded from previous work (Wayne and Cotts, 1966; Robertson, 1966) that for the idealized cases of spherical, cylindrical, and planar bounded diffusion, the Gaussian phase distribution assumption remained valid. The diffusion equation

$$\frac{\partial P}{\partial t} = -D\nabla^2 P$$

was then solved for the aforementioned ideal geometries. The solution to the differential equation for the case of spherically-bounded diffusion was found to be

$$ln\left[\frac{M(2\tau,G)}{M_0}\right] = -\frac{2\gamma^2G^2}{D}\sum_{m=1}^{\infty}\frac{\alpha_m^{-4}}{\alpha_m^2R^2-1}\left(2\tau - \frac{3-4\exp(-\alpha_m^2D\tau)+\exp\left(\alpha_m^2D2\tau\right)}{\alpha_m^2D}\right)$$

where R is the radius of the sphere, and α_m is the mth root of

$$\alpha_m RJ'_{\frac{3}{2}}(\alpha_m R) - \frac{1}{2}J_{\frac{3}{2}}(\alpha_m R) = 0$$

where $J_{3/2}(x)$ is the Bessel function of order 3/2. The time evolution of this magnetization decays with a time constant equal to

$$\frac{1}{T_{2D}} = -\frac{2\gamma^2GR^4}{D}\sum_{m=1}^{\infty}\left[\frac{1}{\alpha_i^4(\alpha_i^2-2)}\left(1-\frac{3-4\exp\left(-\frac{\tau{\alpha_m}^2D}{R^2}\right)+\exp\left(-\frac{2\tau{\alpha_m}^2D}{R^2}\right)}{\frac{2\tau{\alpha_m}^2D}{R^2}}\right)\right]$$

which is the expression for diffusion relaxation time posited without rationale in Chapter 1. This equation collapses to the Carr and Purcell equation for diffusion relaxation time in the limit where τ is long compared to the time required for proton spins to diffuse between boundaries.

2.2 ADVANCED NMR ANALYSES

2.2.1 Simultaneous T_1-T_2 Measurements

The Carr and Purcell method for measuring T_2 was improved upon by Meiboom and Gill (1958) by ensuring coherence of the successive 180° pulses in the RF pulse sequence and shifting the phase of the 90° pulse by 90° with respect to the 180° pulses. These modifications ensured more sound and repeatable measurement of T_2 via the method of Carr and Purcell. While the Carr-Purcell-Meiboom-Gill (CPMG) method and corresponding T_1 measurement (inversion recovery) are imperfect (ex. Putte, 1970; Jones, 1972), they have normally been considered accurate techniques for measuring relaxation times. As pointed out by Sezginer et al. (1991), however, inversion recovery is time consuming when longitudinal relaxation is long or the signal-to-noise ratio is low. Other methods have been developed to hasten the acquisition of longitudinal relaxation time data. Garwin and Reich (1959) first recognized that several 90° pulses could be applied to eliminate net magnetization, then recovery time toward the equilibrium state could be observed (a technique called "saturation recovery"). This technique was explored by others (e.g. Markley et al, 1971; McDonald and Leigh, 1973), especially for use in NMR chemical spectroscopy. Another method, called "fast-inversion-recovery," was developed by Canet et al. (1975). This technique modified the inversion recovery experiment using inter-scan waiting times less than $5T_1$, as in a saturation recovery experiment. This introduced a slightly more complicated inversion for T_1 but provided faster longitudinal relaxation time measurement. This technique was noted by Sezginer et al. to be the most efficient way of measuring longitudinal relaxation. Sezginer et al. presented a variation of fast-inversion-recovery that replaced the monitor RF pulse (the single 90° pulse used for pulse-tipping and signal acquisition) with a full CPMG sequence. At the end of each CPMG sequence, the net longitudinal and net transverse magnetization becomes zero,

allowing for a consistent end-state in which to begin a new measurement cycle. This per-cycle pulse sequence combination of fast-inversion-recovery (T_1) and CPMG (T_2) allows for measurement of T_1 and T_2 simultaneously.

Sezginer et al. noted the advantage of shorter acquisitions times in fluids using the fast-inversion-recovery/CPMG method. However, an additional important utility of simultaneous T_1-T_2 measurements is the ability to identify fluid populations with combinatorial transverse-longitudinal relaxation times. In other words, the fraction of the total fluid volume occupied by regions of given T_1-T_2 combinations can be extracted using a simultaneous measurement method. Peemoeller and Shenoy (1981) employed a similar approach for measuring T_1 and T_2 simultaneously, and was the measurement technique employed in the present work. These types of measurements allow for more advanced analysis of pore system properties using T_1-T_2 computed attributes (for example, the ratio T_1/T_2, or the one introduced in the following section).

2.2.2 Secular Relaxation Time

NMR relaxation that occurs which is not caused by bulk fluid processes and surface interactions, but by other or "non-natural" processes, as they were called by Carr and Purcell (1954) and others (ex. Kleinberg and Horsfield, 1989), is typically due to diffusion of proton magnetic moments through heterogeneities in the local magnetic field which cause irreversible loss in the phase coherence of precessing magnetic moments. This includes diffusion relaxation, but non-natural processes also include the effects of how paramagnetic interactions affect longitudinal and transverse relaxation differently, i.e., due to the effect of scalar coupling on T_2 (Kleinberg et al., 1994). The sum of these effects has been characterized by a relaxation rate termed "secular" relaxation (Slichter, 1978) and is defined by the difference in transverse and longitudinal relaxation rates:

$$\frac{1}{T_{2sec}} = \frac{1}{T_2} - \frac{1}{T_1}$$

As described in **S2.1**, different methods have been developed to mitigate the decrease in transverse relaxation time due to the effect of diffusion. However, sufficiently rapid diffusion of protons in the presence of large paramagnetic or ferromagnetic species can still lead to a prevailing secular response. Therefore, analysis of secular relaxation may yield useful information in rocks containing minerals of this type. Theoretical models of secular relaxation have been developed for various ideal magnetic field distributions (Gillis, 1987) and as a function of the diffusion rate, inter-echo half-spacing τ, and pore geometry (Anand and Hirasaki, 2008). These results have proven useful, for example, in determining the size of paramagnetic relaxation centers in unconventional pore systems (Daigle et al., 2014).

2.3 IMAGE ANALYSIS FOR POROUS MEDIA

2.3.1 Medial-axis Skeletonization

Image skeletonization involves reducing a two-phase image into connected paths equidistant from boundaries present in the original image. One type of skeletonization, called "3-dimensional medial-axis" (3DMA), has been developed as an algorithm to aid in feature extraction for image analysis applications (Lee, 1994). Lindquist et al. (1996) applied this algorithm to porous media by replacing the void structures of images of a Berea sandstone and a Danish chalk with 3D medial axis skeletons, which were then analyzed to extract tortuosity distributions and disconnected pore volumes within the samples. Lindquist and Venkatarangan (1999) used an improved 3D medial axis (3DMA)

analysis on microtomographic images of a Fontainebleau sandstone. Introducing a type of nodal analysis to distinguish between pores and pore throats (Figure 2.2), vesicle sizes and vesicle-vesicle contact areas were determined for the sandstone images. A more sophisticated software whose development was seeded by these studies, called 3DMA-rock, can be used to employ more advanced pore throat-searching algorithms and construct pore-throat networks from stacks of segmented and binarized images (Lindquist and Prodanovic, 2004).

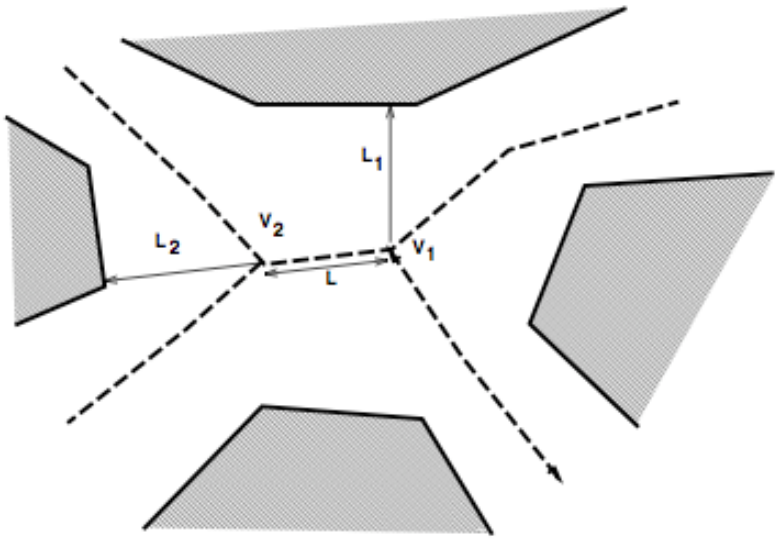

Figure 2.2 from (Lindquist and Venkatarangan, 1999): Medial axis analysis was used to extract a skeleton from images of Fontainebleau sandstone. Pores and pore throats were then ascertained by setting conditions that compared node-node distances and boundary-node distances.

2.3.2 Image Analysis and NMR

Pore sizes are important descriptors of morphology in porous media, and often have a strong bearing in calculations of petrophysical properties. Nuclear magnetic resonance T_1 and T_2 spectra represent distributions of surface-to-volume ratios within a pore system, given that the distributions are properly attuned via a secondary empirical technique. The fast-diffusion formulation of NMR relaxation suggests that relaxation time is directly proportional to pore size by a constant of proportionality called surface relaxivity. Surface relaxivity can be determined by correlating the NMR distribution with another measure of pore size. Often this is done using mercury injection porosimetry (MICP) (e.g. Daigle et al., 2014). However, other measures of pore size should theoretically suffice as well. A limitation of MICP is that it is difficult to characterize, such that it measures pore throat sizes weighted by intruded pore volumes (Coates, 1999). Studies using micro-CT image analysis results for comparison with NMR distributions are uncommon, but have been carried out by Padhy et al. (2006) and Arns (2004). Padhy et al. used micro-CT-derived pore size distributions to evaluate a less-common NMR technique called "decay due to diffusion in internal field" (DDIF-NMR). The objective was to determine the method's feasibility as a wide-scale pore size distribution determination technique, applied to synthetic vuggy media. Arns et al. employed micro-CT image analysis to extract a distribution of pore sizes for two sandstones, a carbonate rock, and a dual-scale reservoir rock. He then modeled NMR responses according to three different models and compared the results. To the knowledge of this author, no direct correlations of micro-CT data and NMR measurements have been carried out, nor their comparisons with MICP-correlated results.

Chapter 3: Methodology

This chapter details the equipment, experimental techniques, and analytical methods employed to obtain NMR and image analysis data and results. Included are the basic features and parameters of the NMR core analyzer and software, micro-CT facility and image acquisition information, and an explanation of the experimental techniques employed to collect NMR data. Analysis of micro-CT data using image analysis software is described, as are the algorithms employed to extract pore system information from analyzed CT image stacks. Methods for obtaining pore system information from NMR data are also explained using both the standard fast-diffusion assumptions and a more advanced technique, called secular relaxation analysis.

The methods used to employ a restricted diffusion model to extract pore system properties, including population-specific internal magnetic field gradients and surface relaxivities, are described.

3.1 Equipment and Empirical Techniques

3.1.1 NMR Equipment and Experimental Method

Nuclear magnetic resonance experiments were conducted using a GeoSpec2 benchtop core analyzer hardware and software system developed by Oxford Instruments and Green Imaging Technologies (Figure 3.1). The operating frequency of the GeoSpec2 is 2 MHz, but the system may be calibrated for NMR frequencies of up to 12 MHz. The system accepts core sample diameters less than 52 mm. The proton resonant frequency corresponded to a static magnetic field strength of 0.05 T with a gradient of 0.21 mT/m (Daigle et al., 2014).

Figure 3.1: The GeoSpec2 core analyzer NMR system. Core samples were placed in a sample tube and lowered into a cylindrical cavity containing the NMR magnet. The operating frequency was 2 MHz with a static magnetic field strength of 0.05 T and a gradient of 0.21 mT/m.

NMR experiments were performed on brine-saturated rock cores. Dry 1" diameter, 2" length core samples of Berea sandstone, Boise sandstone, Silurian dolomite, and were obtained. Samples were placed in a glass vacuum chamber and evacuated for 4.5 hours using a Welch® 1400 DuoSeal® vacuum pump. A solution of 3.5 wt% NaCl brine was then introduced into the chamber until the cores were fully submerged in brine. Additional vacuuming was performed for 35 minutes.

Saturated cores were stored in a brine bath and kept in an isolated glass chamber to minimize contamination until NMR experiments were ready to be conducted. To prevent desiccation of each core sample during the NMR experiment, each sample was tightly wrapped in polyethylene and sealed with a paraffin film before each test. Both the polyethylene and paraffin film were determined to have negligible intrinsic NMR signals (Daigle et al., 2014). The sealed core was placed into a glass sample tube and positioned

inside the NMR magnet. The GIT Systems software package was used to select NMR test parameters, including test type, echo half-spacing τ, and signal-to-noise ratio.

3.1.2 Micro-CT Facilities Specifications

Micro-CT image stacks were obtained from the University of Texas High Resolution X-ray CT facility (UTCT) using the XRadia MicroXCT 400 scanner. The instrument uses cone-beam acquisition for rapid scanning and employs a Hamamatsu X-ray source with an energy range of 40 to 150 kV. The voxel resolution of the instrument is dependent on the size of the sample to be scanned. Each image slice was composed of 1024 x 1024 pixels. The voxel resolution of the 1" diameter Silurian dolomite sample was therefore 26.5 microns. A smaller 0.08" x 0.16" Berea sandstone core was also imaged at a voxel resolution of 4.25 microns due to its smaller dominant pore size.

3.2 Micro-CT Image Analysis

Example micro-CT slices from the image stacks of Berea sandstone and Silurian dolomite are shown in Figure 3.2. The first-order objective in the analysis of the image data was to clean and segment the images. This involved removal of noise from the images and a binarization of the image grayscale into black and white (pore and grain) phases. The image processing package Fiji, a plugin-bundled version of ImageJ, was used to perform these operations.

A two-voxel radius median filter was applied to the samples to reduce noise in the data for improved thresholding and edge detection (see Figure 3.3, panels 1 and 2). A median filter was selected for its effectiveness in smoothing fine features while preserving edge structures. This filter was particularly useful in removing speckling noise, which was observed in the original images of the Berea and Silurian samples.

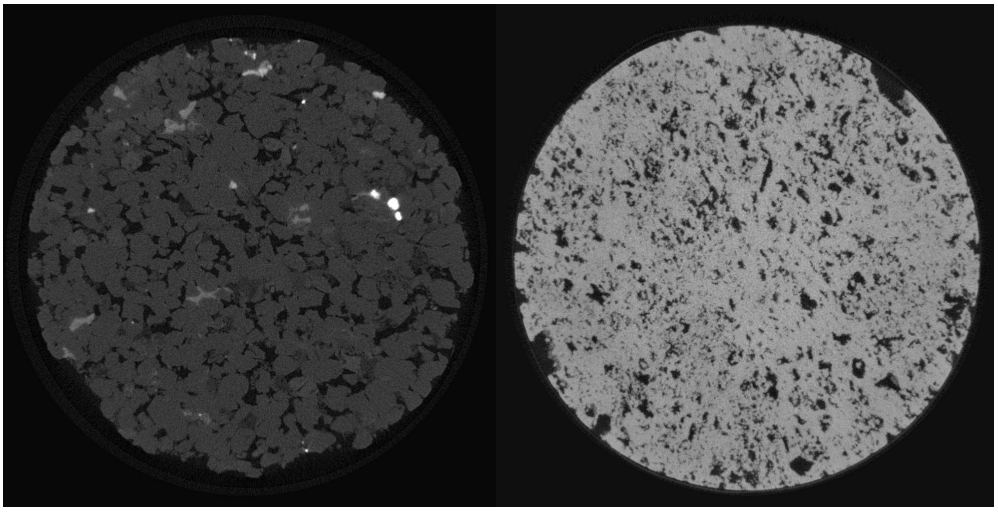

Figure 3.2: Example X-ray CT image slices from the image stacks of Berea sandstone (left) and Silurian dolomite (right). The pixel resolutions of the Berea and Silurian images were 4.65 μm and 26.5 μm, respectively.

Delineation of grain edges was performed using a calibrated simple thresholding technique. Grain edges appeared in images as grayed boundaries spanning several voxels and thus definitive selection of pore-grain boundaries was not evident. This complicated clean segmentation of the images into grain and pore phases. Furthermore, unresolved microporosity manifested as intermediate gray values that could be ambiguously construed as either grain matter or pore space. This issue was resolved by obtaining independent measurements of sample porosities from NMR fluid volume measurements and sample dimensions. The grayscale grain cutoff values were then calibrated such that image porosities matched measured porosities. An example slice that has undergone such thresholding is shown in Figure 3.3, panel 3.

Additional post-segmentation cleaning was performed using 3DMA-rock software (Lindquist et al., 2004). A routine that detected small, spatially isolated voxel clusters was used to convert noisy or disconnected voxels to the surrounding phase (Figure 3.4).

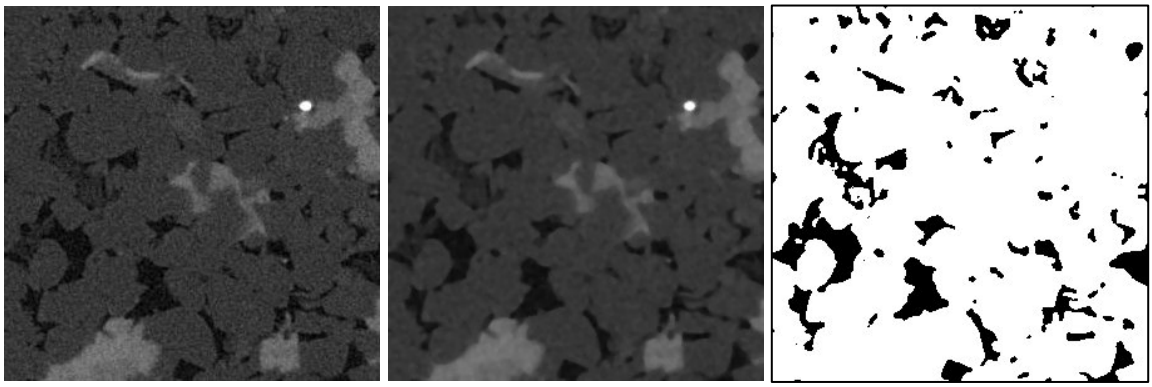

Figure 3.3: An example slice of Berea sandstone that has undergone cleaning and segmentation. Panel 1 (left) shows the original image, panel 2 (middle) shows the image after application of a median filter, and panel 3 (right) shows the image after undergoing calibrated simple thresholding.

The software package 3DMA-rock was used to extract pore system information from the cleaned and binarized image stacks. A skeletonization method called 3D medial axis was employed, which extracted only structural and topological features from the images. The medial axis skeletons were then used to identify pore-throat networks. Medial axis junction points and pore-pore links were interpreted as pore bodies and pore throats, respectively.

Construction of the medial axis network was performed using the "grassfire" algorithm (Figure 3.5). In each 3D binarized image, the algorithm started a "fire" of voxels at each grain surface (binary = 1), and then burned in a direction normal to each boundary. At the meeting point of any two burning voxels, the burn iteration was ceased and a medial axis candidate was established. Post-processing medial axis cleanup removed extraneous axis features.

Algorithms were employed to distinguish pore and pore-throat structures along the medial axis skeleton. The 3DMA-rock software offered multiple so-called "throat-finding" procedures; the Dijkstra-based throat search and the Wedge-based throat search

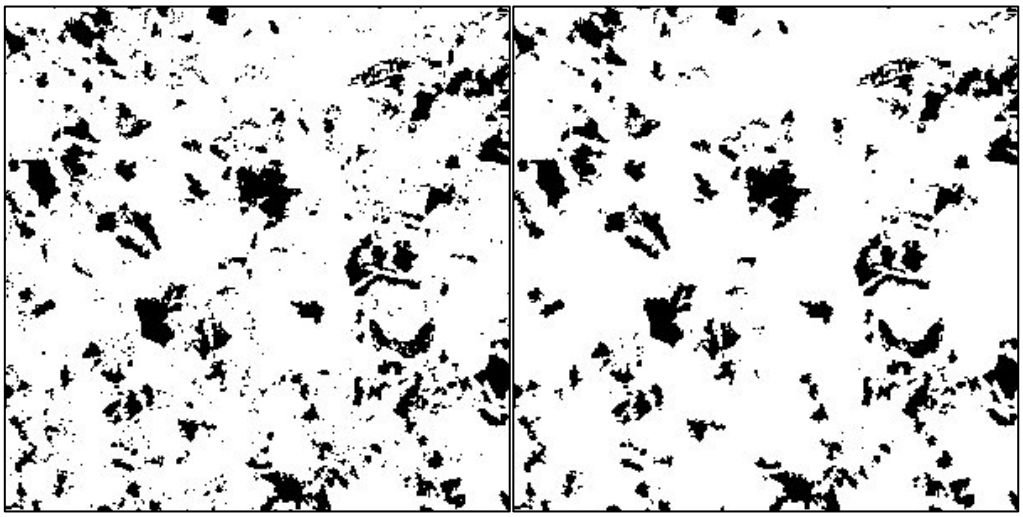

Figure 3.4: An example of the 3DMA-rock cleanup routine. The phases of small isolated clusters of voxels were reversed as a method of noise reduction.

were employed for this purpose. The Dijkstra search generated dilating rings of voxels normal to the medial axis. Each ring voxel was frozen once it encountered a grain boundary, and the algorithm continued until an unbroken frozen path about the medial axis was ascertained. The cross-sectional area enclosed by each path was calculated by triangulation of the perimeter voxels with the medial axis voxel, and the plane of minimum cross section was selected as a throat.

The Wedge-based approach considered wedge-shaped sections about each medial axis path voxel. Starting with the most proximal grain voxel, it computed a perimeter cross section based on the sum of the areas of the wedges. The plane with minimum cross section along the medial axis was selected as the throat in this case.

A pore-throat network was constructed from the information gleaned from throat-searching the medial axis via Dijkstra and Wedge algorithms. Superposition of pore-throats and pores ascertained on the medial axis with binarized image data allowed

enumeration of voxels per pore. The number of voxels in each pore represented the size of that pore. Pore size frequency distributions were thus extracted for each sample.

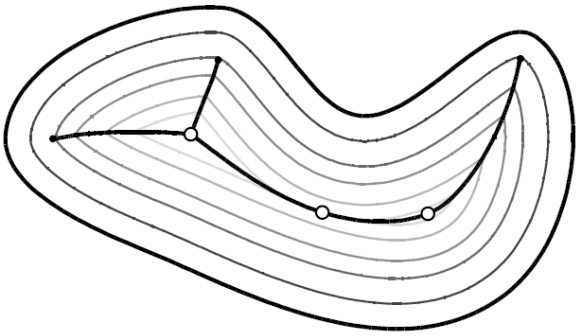

Figure 3.5: The grassfire algorithm burned voxels in a direction normal to the grain boundaries at each iteration. At each meeting point of two burning voxels, a medial axis candidate was established. The resulting skeleton was analyzed to extract structural and topological information for the system.

3.3 NMR Analysis Techniques

3.3.1 Surface Relaxivity Cross-Correlation

The fast-diffusion NMR relationships

$$\frac{1}{T_1} = \rho_1 \left(\frac{S}{V}\right)_{pore}$$

$$\frac{1}{T_2} = \rho_2 \left(\frac{S}{V}\right)_{pore}$$

allow pore size distributions to be computed from NMR T_1 and T_2 distributions. This is done by employing a second experimental method and comparing to NMR data to obtain surface relaxivities ρ_1 and ρ_2. The experimental method can be mercury-injection porosimetry (MICP), nitrogen absorption experiments, image analysis, or some other measure of pore size distribution (see Section **S1.2.3**). Once a pore size distribution is obtained, the T_1 or T_2 distribution can be cross-correlated with the pore size distribution to extract ρ_1 and ρ_2. Each NMR distribution shifted by its corresponding surface relaxivity factor represents a pore size distribution containing information from both experiments. Surface relaxivity values are obtained by maximizing the cross-correlation function

$$C(\rho_{1,2}) = \int_{-\infty}^{\infty} \alpha_{1,2}(t)\beta_{1,2}(t)dt$$

where $\alpha_{1,2}(t)$ represents the T_1 or T_2 distribution at time t and $\beta_{1,2}(t)$ represents the empirical pore size distribution expressed as a time series (i.e., at time $t = r/2\rho_{1,2}$) (Marschall et al., 1995). The MATLAB function xcorr was employed to maximize $C(\rho_{1,2})$.

3.3.2 Analysis Using the Restricted Diffusion Model

Secular relaxation distributions were determined from simultaneous T_1 -T_2 measurements. Simultaneous measurement of T_1 and T_2 using the Geospec2 NMR core analyzer returned surface mappings characterizing the fluid volume exhibiting each T_1-T_2 relaxation time pair. Figure 3.6 shows a visualization of such a measurement for a sample of Silurian dolomite. Brighter blue peaks correspond to greater fractions of total fluid volume exhibiting a particular T_1-T_2 relaxation time combination. To extract a distribution of secular relaxation times from this data, secular relaxation time, defined by

$$\frac{1}{T_{2sec}} = \frac{1}{T_2} - \frac{1}{T_1}$$

was computed for each T_1-T_2 pair in the domain probed by the analyzer. Fluid volumes were then binned into a range of secular relaxation times ranging from 10^{-2} ms to 10^4 ms. Divergent and negative values of secular relaxation were discarded and the remaining fluid volume renormalized to its nominal value. This process was performed for twenty-two tests; two samples at each of five different τ and two additional samples at each of six different τ. Values of τ were in the range from 0.052 ms to 0.600 ms.

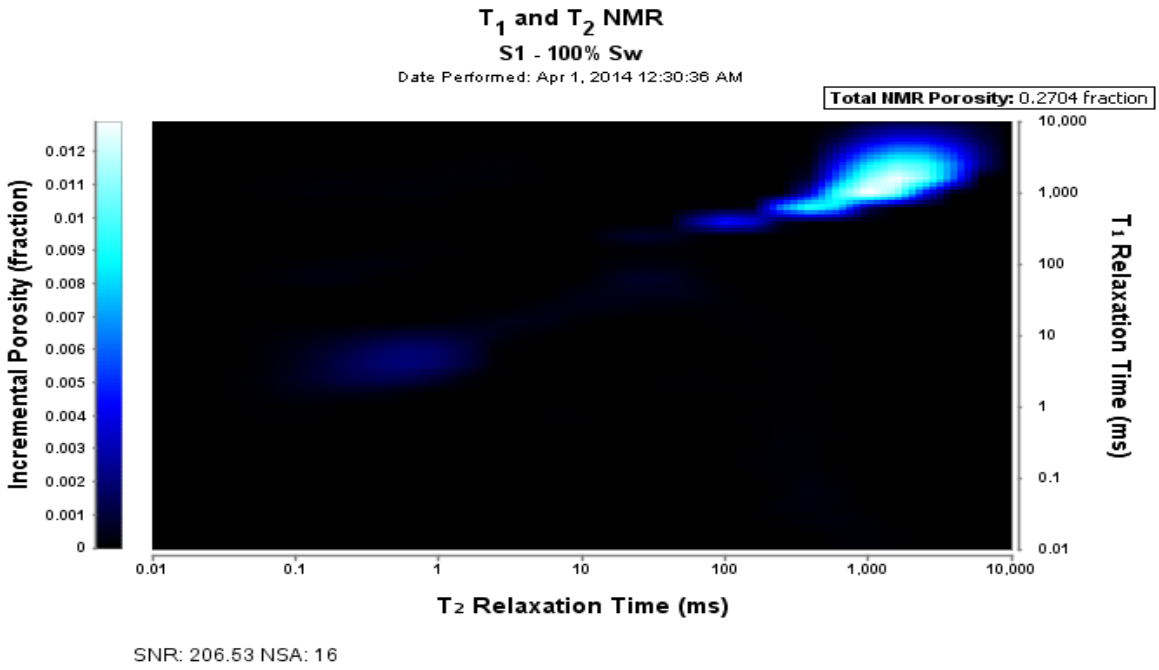

Figure 3.6: An example of simultaneous T_1-T_2 data for Silurian dolomite. Bright blue peaks correspond to greater fluid volumes with given measured T_1-T_2 combinations. Secular relaxation data were determined from simultaneous NMR measurements.

The first secular relaxation analysis involved extraction of internal field gradients using the restricted diffusion model. In theory, the effects of surface relaxation and bulk relaxation do not change when otherwise identical experiments are run with different τ. Therefore, the difference between two secular relaxation measurements should depend only on relaxation due to diffusion.

This can be expressed as

$$\frac{1}{T_{2\text{sec}}(\tau_2)} - \frac{1}{T_{2\text{sec}}(\tau_1)} = \frac{1}{T_{2D}(\tau_2)} - \frac{1}{T_{2D}(\tau_1)}$$

where the terms on the left hand side represent the difference in two secular relaxation measurements at two different τ and the terms on the right hand side represent the difference in diffusion relaxation at the same two τ.

Variation of T_{2D} in a spherical pore as a function of echo spacing and other parameters was presented in **S1.2.4**. In this formulation it was shown that diffusion relaxation depends on echo spacing, internal magnetic field gradient strength, pore size, and fluid self-diffusion coefficient. The secular relaxation rate ($1/T_{2sec}$) was observed as a function of echo spacing for each sample. Least-squares best-fit lines were then superposed through the datasets **(S4.2.2)**. Secular relaxation was characterized from each best-fit line at the maximum and minimum τ and was used compute $1/T_{2\mathrm{sec}}(\tau_2)$ and $1/T_{2\mathrm{sec}}(\tau_1)$, respectively. Diffusion relaxation values $1/T_{2D}(\tau_2)$ and $1/T_{2D}(\tau_1)$ were then modeled for the same τ, using pore sizes gleaned from image analysis for Silurian dolomite and Berea sandstone, from literature for Boise sandstone, and assumed to be roughly equal to bead radius for the bead pack. The restricted diffusion model for T_{2D} was optimized as a function of G to match the rates of change revealed by the slopes of the least squares lines.

The second secular relaxation analysis modeled both surface and diffusion relaxation components in parallel to invert for pore size (R) and the difference in transverse and longitudinal surface relaxivities ($\Delta\rho = \rho_2 - \rho_1$). Internal magnetic field gradients obtained from the previous analysis were used in this investigation. The parallel adding rule presented in **S1.2.4** was used in conjunction with the restricted diffusion model to extract surface relaxivities and volume-weighted mean pore sizes. Expressed in parallel with diffusion relaxation, secular relaxation time can be expressed as:

$$T_{2sec,mod,i} = \left(\frac{3(\rho_2 - \rho_1)}{R} + \frac{1}{T_{2D}(\tau_i, R)}\right)^{-1}$$

where the relaxation time subscript *mod,i* indicates secular relaxation time modeled at the *i*th echo half-spacing value. Given measured secular relaxation times $T_{2sec,meas,i}$ characterized at each echo half-spacing i by the weighted mean value of the data, a two-dimensional χ^2 analysis can be performed, where

$$\chi^2 = \sum_{i=1}^{n} \frac{\left(T_{2sec,mod,i} - T_{2sec,meas,i}\right)^2}{(T_{2sec,mod,i})^2}$$

is minimized as a function of model parameters. Thus a two-dimensional parameter space was generated, defined in the y-dimension by the difference in surface relaxivities $\Delta\rho = (\rho_2 - \rho_1)$ and in the x-dimension by pore size R. A fine-mesh domain of values was constructed, bounded by physically reasonable lower and upper bounds (i.e., 1 to 100 μm/s for $\Delta\rho$, and 1 to 200 μm for R). For each point in the parameter space, a χ^2value was computed. The parameter combination corresponding to the minimum χ^2value was selected as the best-fit value pair.

Sensitivity analysis was performed by introducing Gaussian white noise to the model. Modeled values were deviated by an amount randomly chosen for cases of a 0.05σ and a 0.10σ normally-distributed number generator. Minimized χ^2 best-fit parameters were then compared to the unperturbed solutions to probe solution stability.

Chapter 4: Data and Results

4.1 Image Analysis Results

The 3DMA software is able to produce medial axis skeletons from processed image stacks using the grassfire algorithm described in **S3.2**. Post-cleanup medial axis skeletons are shown in Figures 4.1-4.3. Skeleton tract colors represent distances of skeleton voxels from pore-phase boundaries. The grassfire algorithm iterates a moving "fire" front of voxels outward from grain-phase boundaries until two fronts meet, extinguish, and establish a skeleton voxel. The more iterations required for extinguishment, the more reddish the voxel color on the medial axis skeleton. These colors are represented in code by "burn numbers," which are important in delineating pores from pores throats when constructing a pore-throat network.

Algorithms were next executed to consider the axes in the context of the segmented (two-phase) three-dimensional image stacks. These algorithms, called the Dijkstra-based and Wedge-based throat finding algorithms, are described in **S3.2**. Each skeletal node, node connection, and its relationship to the original image stack was established. Based on these relationships, nodes and connections were assigned "pore" or "pore-throat" tags. Voxels within each pore were then enumerated as pore volumes. Visualizations of these networks are shown in Figures 4.4-4.6 below. The volume of each pore is visualized by a sphere of proportionate diameter at a spatial location determined by its center-of-mass. The color scheme in these images varies with relative pore size from small (blue) to large (red). Pore throats are represented by straight lines as connections between pore bodies.

Note the single largest pore in the sample of Indiana limestone. The pore-node throat-connector analysis inherent to 3DMA was unable to adequately partition the pore space into discrete pore and pore-throat volumes. This is likely due to the geometry of the

carbonate network, which from these 3DMA results can be interpreted as a single large well-connected system of macropores with associated poorly connected micropores. While this result provides important information about the limestone pore system, its lack of information with regards to the distribution of pore sizes for the majority of the rock porosity makes it less useful for correlation with volumetrically-weighted NMR results. The results obtained for the Indiana limestone image analysis component were therefore omitted from further analyses in this study.

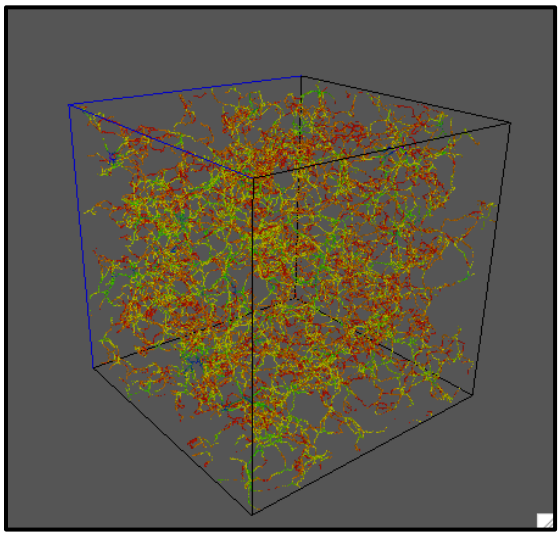

Figure 4.1: Berea sandstone 3D medial axis skeleton produced using 3DMA-rock software. Red skeleton voxels indicate greater distances of the skeleton to the grain boundaries, whereas green skeleton voxels indicate closer proximities to the boundaries and likely narrower geometries.

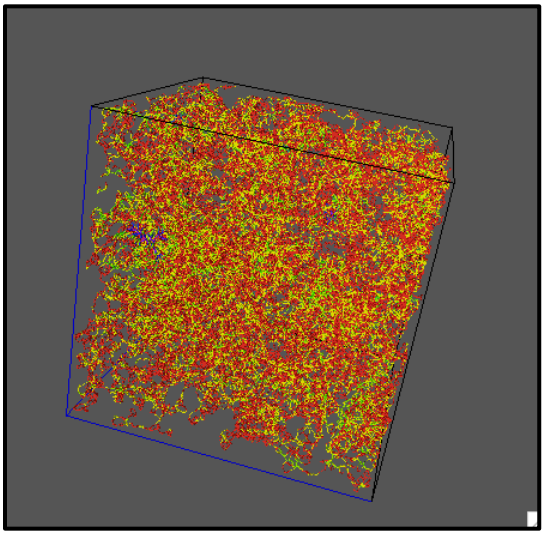

Figure 4.2: Indiana limestone 3D medial axis skeleton produced using 3DMA-rock software. Red voxels indicate larger distances to grain boundaries and green voxels indicate closer proximities to grain boundaries.

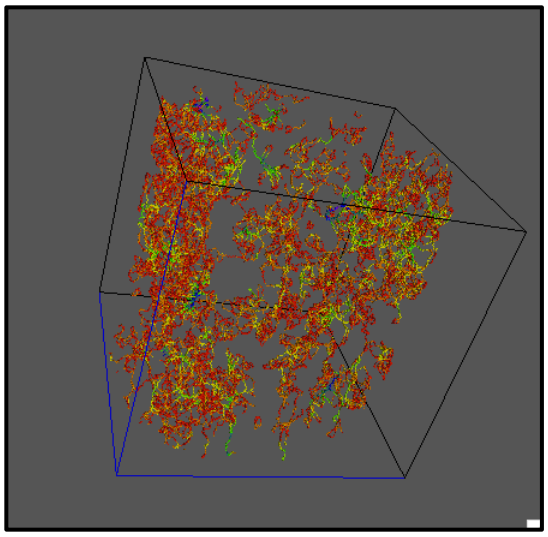

Figure 4.3: Silurian dolomite 3D medial axis skeleton produced using 3DMA-rock software. Red voxels indicate larger distances to grain boundaries and green voxels indicate closer proximities to grain boundaries.

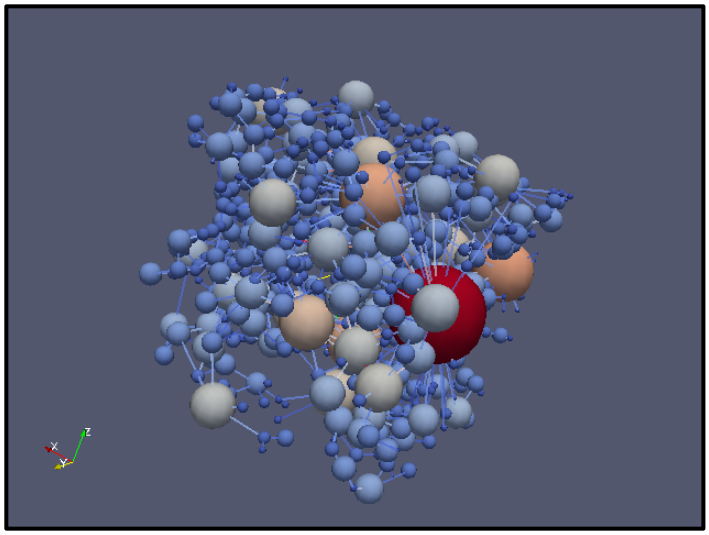

Figure 4.4: Pore-throat network for the sample of Berea sandstone. Pore bodies are represented by spheres of sizes proportionate to body voxel counts. Lines connecting spheres represent pore throat connections. Sphere locations represent center of mass locations of pores.

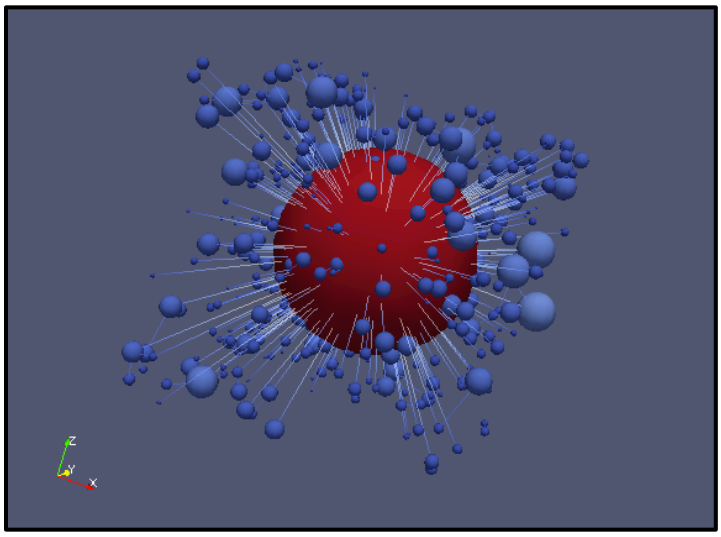

Figure 4.5: Indiana limestone pore-throat network. Pore bodies are represented by spheres of size proportionate to body voxel counts. Pore throat connections are represented by lines connecting the spheres. Note the single dominant pore near the center of the model. This excessively large "pore" likely represents a very large connected volume. In effect, the shapes of the pores in the carbonate network were not amenable to distinction by the Dijkstra and Wedge –based algorithms.

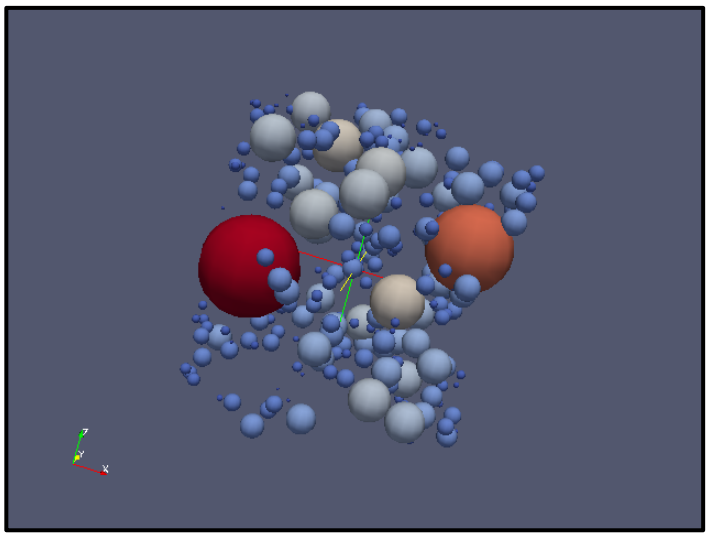

Figure 4.6: Silurian dolomite pore-throat network. Spheres of sizes proportionate to their body voxel counts represent pore bodies. Sphere locations represent the center of mass locations of pores.

4.2 MICP AND IMAGE ANALYSIS NMR CORRELATION RESULTS

Mercury injection porosimetry results were obtained for samples of Berea sandstone and Silurian dolomite. Incrementally intruded volumes of mercury were recorded at each pressure step and reported as the minimum intruded pore size at that step (Figure 4.7), according to the Young-Laplace equation for capillary equilibrium (Young, 1805). Note the sharp singular peaks presented in the MICP data. Mercury injection typically displays a percolation effect that is manifested in a large peak typically displayed in MICP pore size distributions (Katz and Thompson, 1987). Specific smaller pores within the system may control access to larger pores or regions of larger pores. As pressure is increased beyond a critical threshold, a sudden dramatic volumetric intrusion may occur. This large intrusion is reported as a single pore size, when in fact it instead may represent a percolation threshold at which mercury may invade the remaining pore space. It is also important to note that mercury injection is limited by pore throats that control access to pore volumes, and thus MICP is a measure of weighted pore throat size distribution rather than pore body size distribution.

Figure 4.8 shows the distributions of pore sizes obtained from image analysis. The peak pore size was found to be 30 μm for Berea sandstone and 127 μm for Silurian dolomite. The weighted arithmetic mean pore sizes were 41.4 μm for Berea sandstone and 173.1 μm for Silurian dolomite. Pore radius was computed assuming a spherical pore based on total voxel count for each pore. Figures 4.9 and 4.10 show transverse and longitudinal NMR measurements for Berea sandstone and Silurian dolomite. These results were cross-correlated with micro-CT measurements and MICP data according to **S3.3.1**. Figures 4.11 and 4.12 show NMR pore size distributions after cross-correlation with MICP results for Berea sandstone and Silurian dolomite, respectively. Note the secondary, smaller peak at $\sim 10^{-1}$ μm in the NMR pore size distribution (Figure 4.9) that is

unresolved in both the MICP and the image analysis data. This sensitivity of NMR to porosity below imaging or MICP resolution demonstrates one of the technique's advantages. The surface relaxivity values determined from each technique are shown below in Table 4.1. Note that these surface relaxivities correspond to the dominant pore size mode, since smaller modes are unresolved in both MICP and micro-CT data.

Table 4.1: Surface relaxivity values from MICP and μCT cross-correlations

	$\rho_1(\mu m/s)$	$\rho_2(\mu m/s)$
Berea sandstone (MICP)	14.19	20.37
Silurian dolomite (MICP)	8.26	9.44
Berea sandstone (μCT)	62.4	85.6
Silurian dolomite (μCT)	118.9	139.7

Recall that MICP measurements measure pore throat size distribution, while micro-CT analysis enumerates voxels within each pore body. Since the same NMR distributions were correlated with each technique, a comparison of the NMR-derived pore sizes reveals information regarding the pore-to-throat aspect ratios for these samples. Figure 4.13 shows NMR-derived pore sizes from each technique for Berea sandstone. The identical shapes of these curves reflect the fact that each empirical technique was correlated with the same NMR data. The shift between the micro-CT (pore body measurement) and MICP (pore throat measurement) for Berea sandstone was found to be a factor of 4.2 for the transverse measurements and 4.4 for the longitudinal measurements. This can be interpreted as an approximately 4.3:1 body-to-throat aspect ratio for Berea sandstone. Figure 4.14 shows NMR-derived sizes using each technique for

the sample of Silurian dolomite. Using similar reasoning, a shift factor of 14.4 for longitudinal measurements and 14.8 for transverse measurements was derived. This yields a value of approximately 14.6:1 pore body-to-throat aspect for Silurian dolomite.

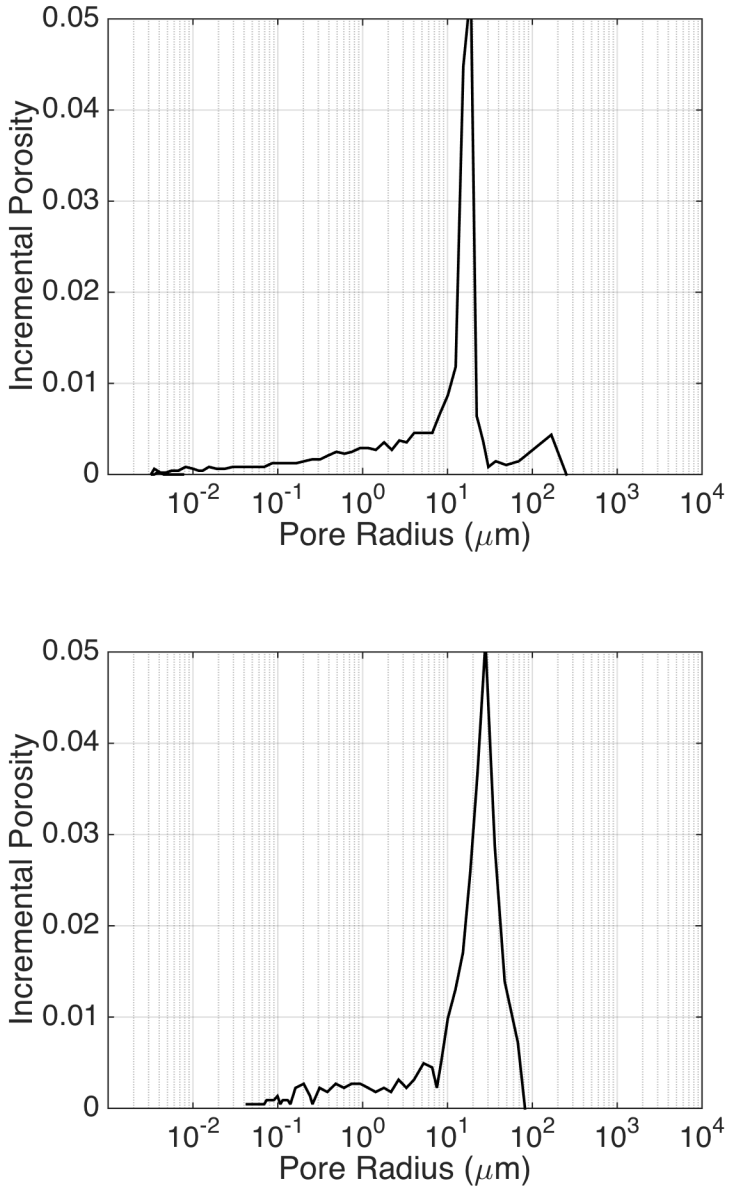

Figure 4.7: Mercury injection porosimetry data for samples of Berea sandstone (top) and Silurian dolomite (bottom). Injection pressure represented as equivalent pore radius is shown versus the intruded volume of mercury at each pressure increment.

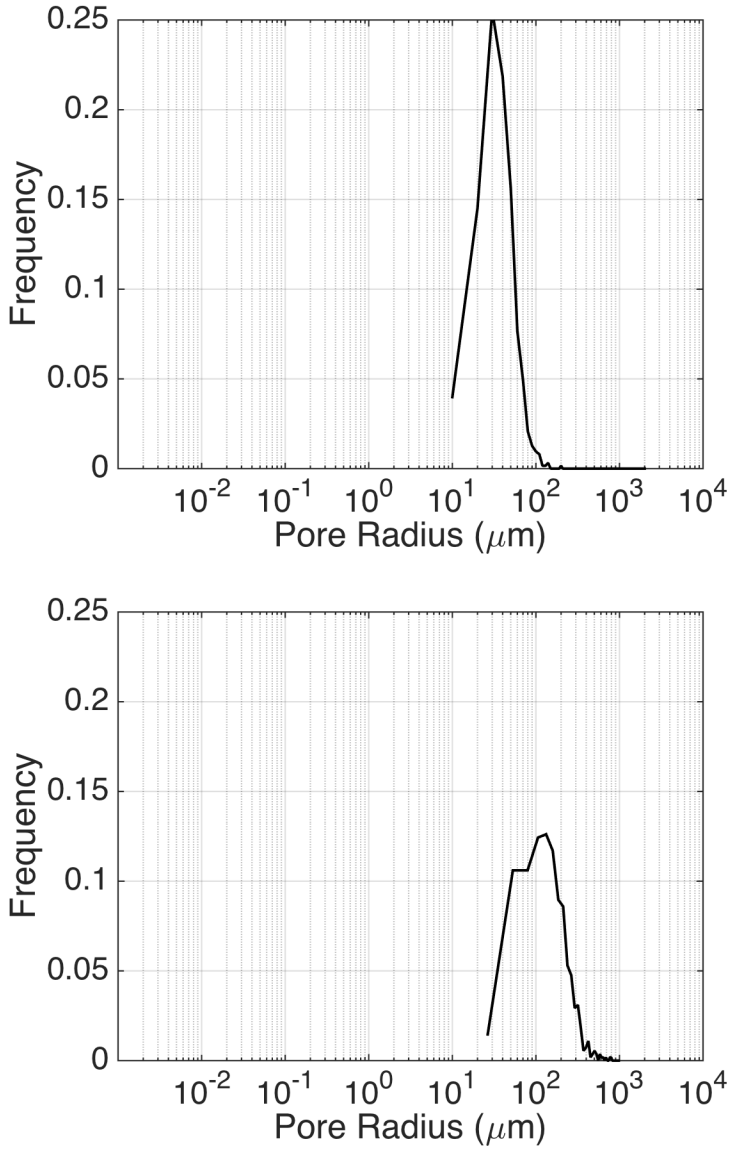

Figure 4.8: Pore size distributions of Berea sandstone (top) and Silurian dolomite (bottom) derived from 3DMA analysis of μCT images. Sizes of voxel clusters identified as pores were assumed spherical and are plotted versus frequency of occurrence in each system.

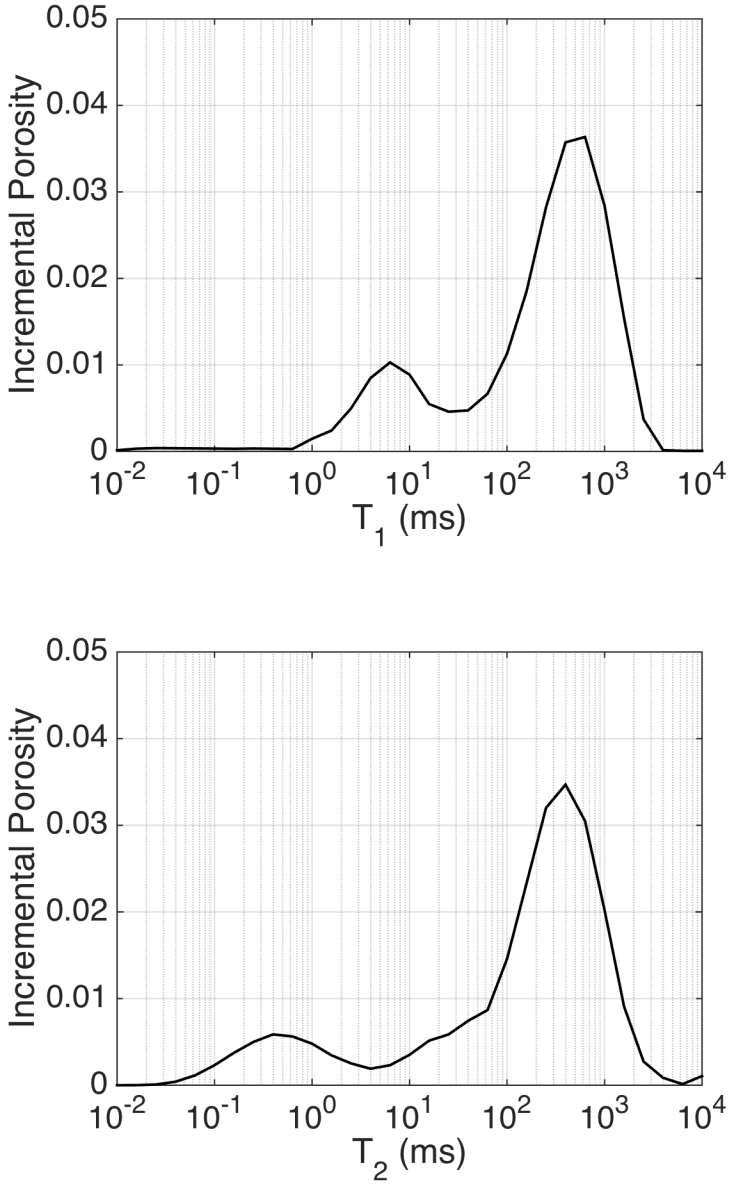

Figure 4.9: Berea sandstone longitudinal (top) and transverse (bottom) NMR measurements. These data can be interpreted as pore size distributions when correlated with image analysis or MICP data. Note the unresolved small pore-size modes in each distribution, which are unresolvable in MICP or image-derived pore size data.

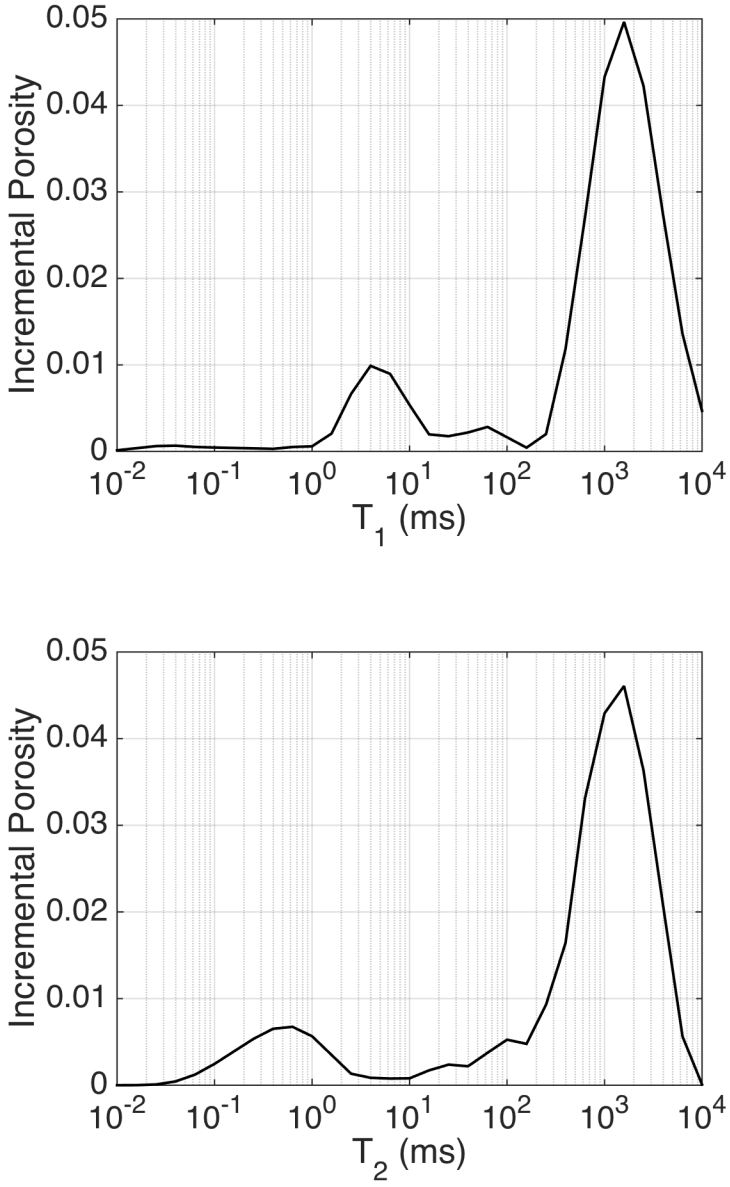

Figure 4.10: Silurian dolomite longitudinal (top) and transverse (bottom) NMR measurements. These data can be interpreted as pore size distributions when correlated with image analysis or MICP data.

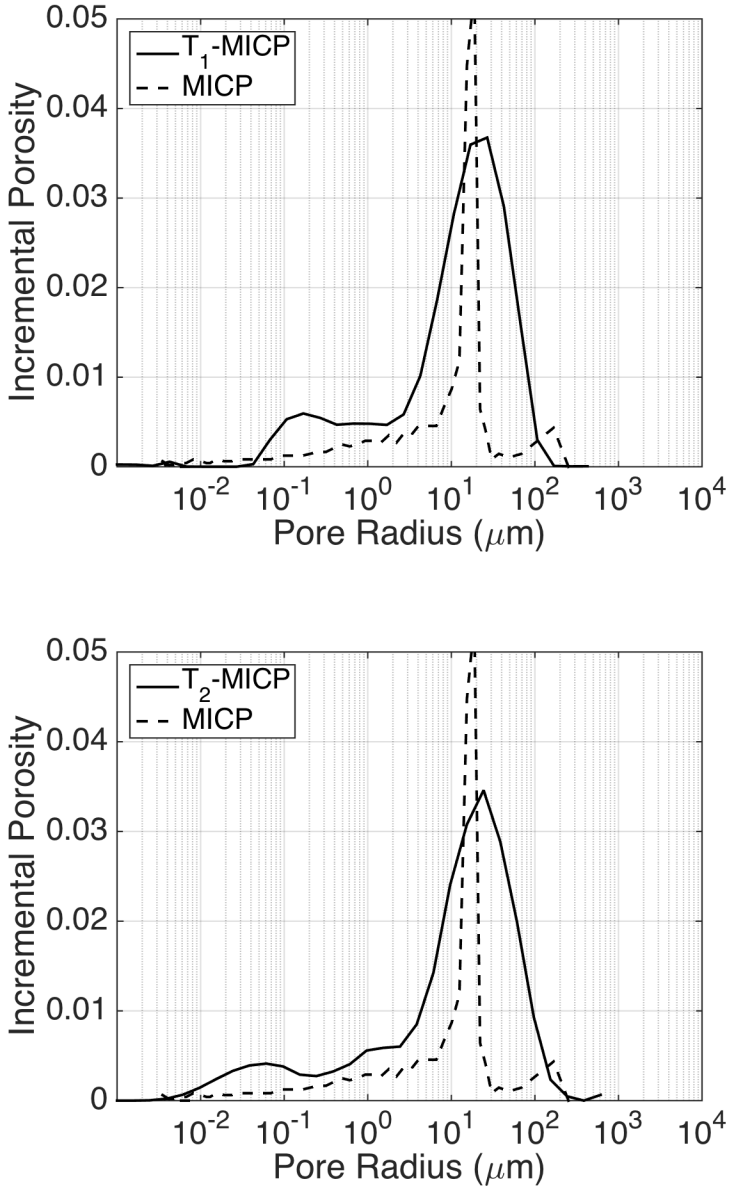

Figure 4.11: MICP-derived NMR pore size distributions for Berea sandstone. Longitudinal (top) and transverse (bottom) measurements were cross-correlated with MICP data to obtain T_1 and T_2 –derived pore size distributions.

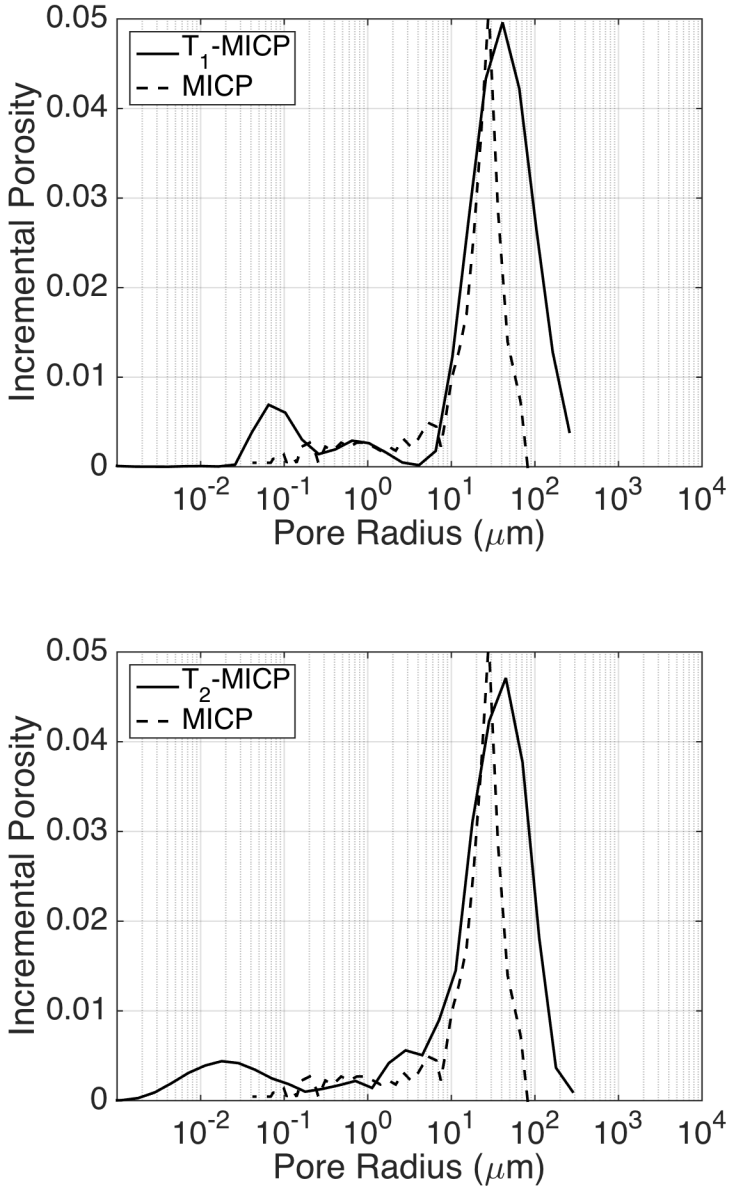

Figure 4.12: MICP-derived NMR pore size distributions for Silurian dolomite. Longitudinal (top) and transverse (bottom) measurements were cross-correlated with MICP data to obtain T_1 and T_2 –derived pore size distributions.

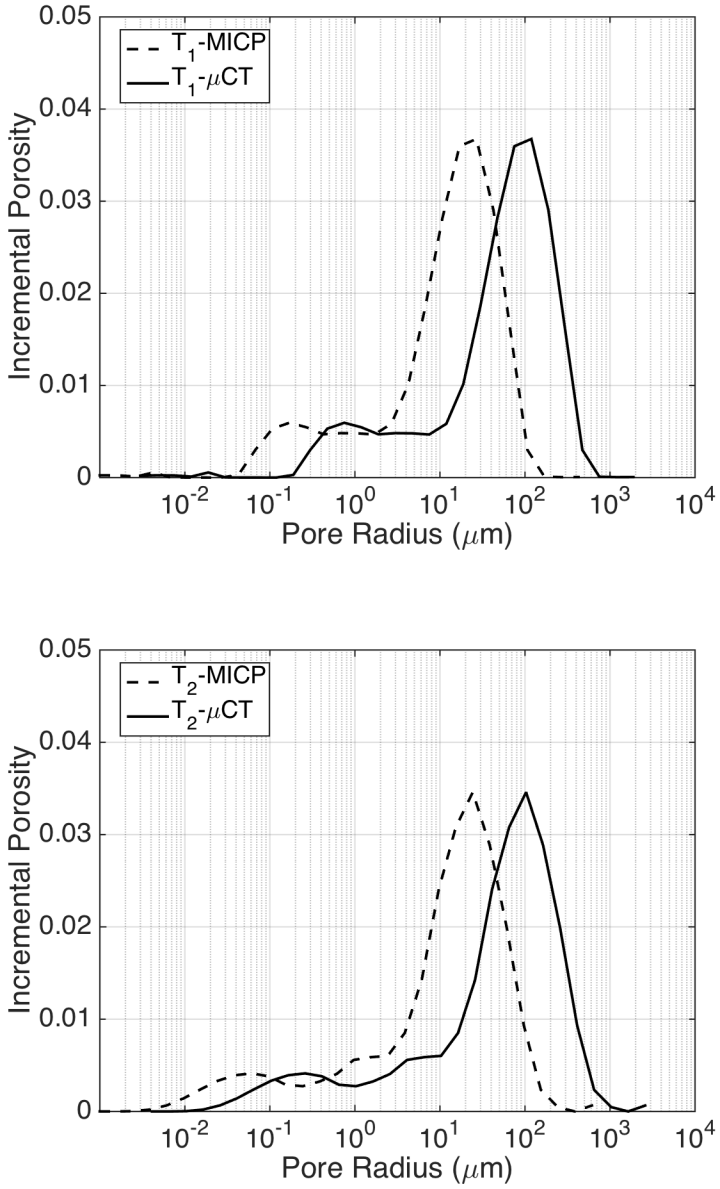

Figure 4.13: Comparison of NMR-correlated pore size distributions using MICP versus μCT pore size data for Berea sandstone. Lateral shifts in longitudinal (top) and transverse (bottom) curves give information regarding pore throat-to-body ratios. An average pore body-to-throat ratio of 4.2:1 was determined for transverse measurements and a ratio of 4.4:1 was found using longitudinal measurements.

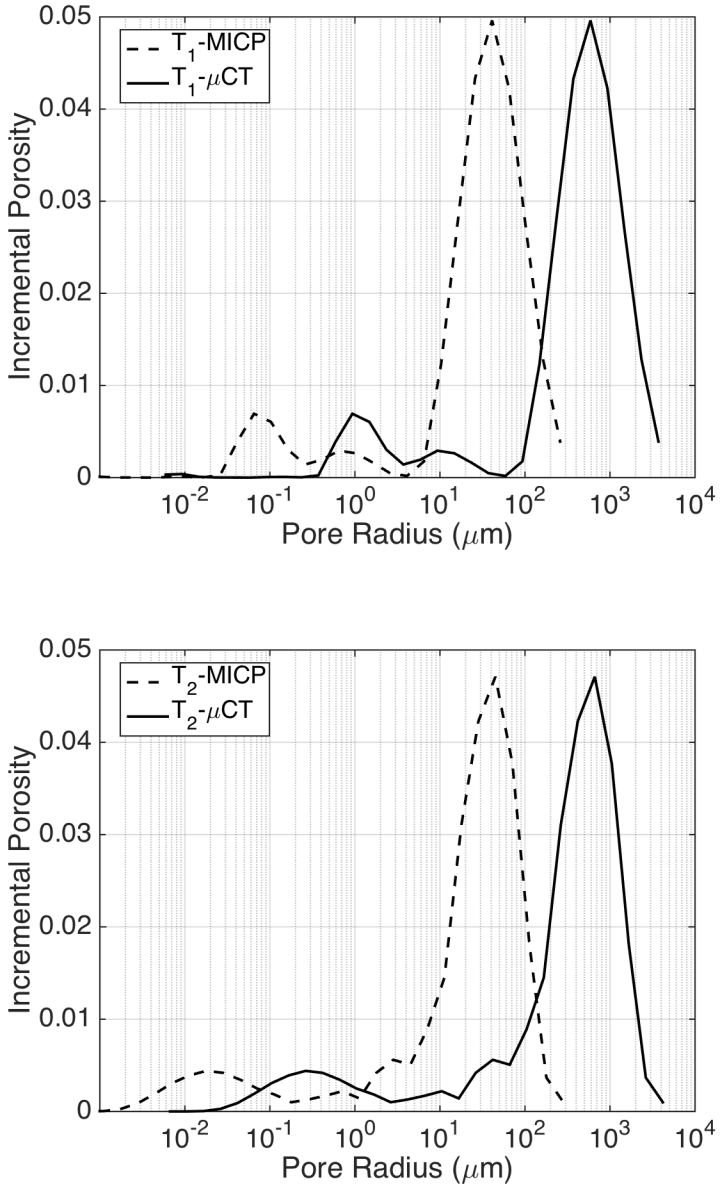

Figure 4.14: Comparison of NMR-correlated pore size distributions using MICP versus μCT pore size data for Silurian dolomite. Lateral shifts in longitudinal (top) and transverse (bottom) curves give information regarding pore throat-to-body ratios. An average pore body-to-throat ratio of 14.4:1 was determined for transverse measurements and a ratio of 14.8:1 was found using longitudinal measurements.

4.3 SECULAR RELAXATION RESULTS

4.3.1 Internal Magnetic Field Gradients

Selected simultaneous T_1-T_2 maps are provided for several τ in Figures 4.15a-d, 4.16a-d, 4.17a-d, and 4.18a-d for the 0.25 mm bead pack, Boise sandstone, Berea sandstone, and Silurian dolomite, respectively. The color scales represent larger fluid volumes in red and smaller volumes in blue. Secular relaxation distributions were determined from these measurements using the method described in **S3.3.2** and are plotted for the four samples in Figures 4.19-4.22. Note qualitatively that the relaxation distributions center on shorter secular relaxation times as τ is increased. This behavior is quantitatively treated by considering variation in the volume-weighted means of these distributions as a function of echo spacing. In **S3.3.2**, changes in diffusion relaxation rate were explained to be proportional to changes in secular relaxation rate. This occurs due to the insensitivity of surface and bulk relaxation rates to changes in τ. Therefore changes in secular relaxation rate can be modeled using Neuman's restricted diffusion model as a function of τ and internal magnetic field gradient G, given that previously determined values of R for each sample and diffusion coefficient D are known as input to the model. Volumetrically weighted mean secular relaxation rate is plotted as a function of τ for each sample in Figures 4.23-4.26. A linear least-squares line is superposed in each figure to characterize the secular relaxation versus τ trends. The endpoints of these lines were matched by the restricted diffusion model by modulating the value of G. A diffusion coefficient for brine of 2.8×10^{-9} m^2/s was used, as were values of R = 173.1 μm for Silurian dolomite and R = 41.4 μm for Berea sandstone from image analysis, a pore size of R = 145 μm for Boise sandstone from SEM images (Krohn, 1998), and R = 125 μm for the radius of the 0.25 mm bead pack. Average internal magnetic field gradient strengths of G = 0.0466 T/m, G = 0.0671 T/m, G = 0.0644 T/m, and G = 0.0265 T/m were

calculated for the bead pack, Boise sandstone, Berea sandstone, and Silurian dolomite, respectively. This method for obtaining magnetic field gradients offers a simple and effective way of extracting volume-weighted average values for porous media using NMR simultaneous T_1-T_2 measurements. Since variations in secular relaxation distributions with echo spacing were observed for all four samples, and corresponding gradient strengths were successfully extracted, it is expected that porous media with gradients at least as large as those present in the least-magnetic sample (Silurian dolomite; $G = 0.0265$ T/m), should also produce responses that can be characterized by this method.

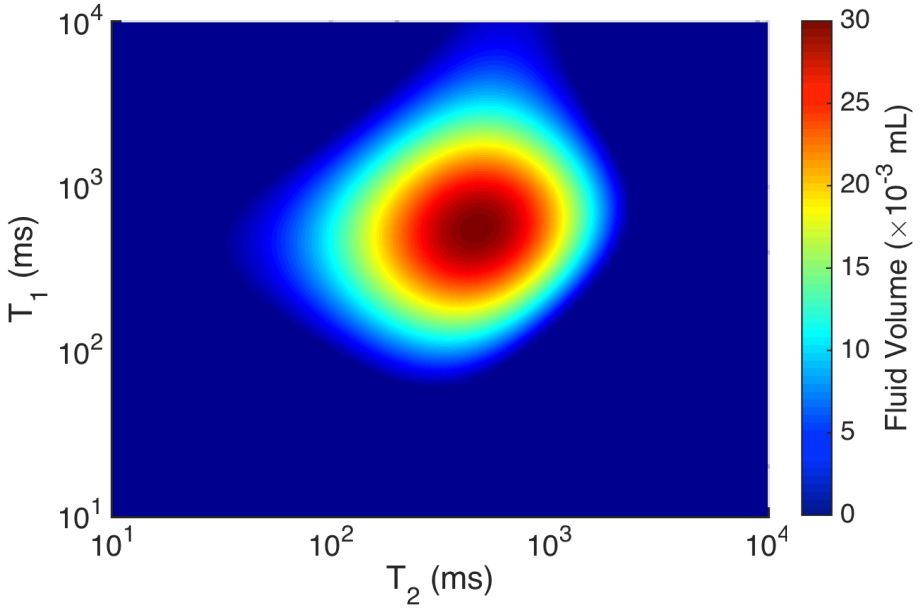

Figure 4.15a: Bead pack (0.25 mm) simultaneous T_1-T_2 NMR map at $\tau = 0.052$ ms.

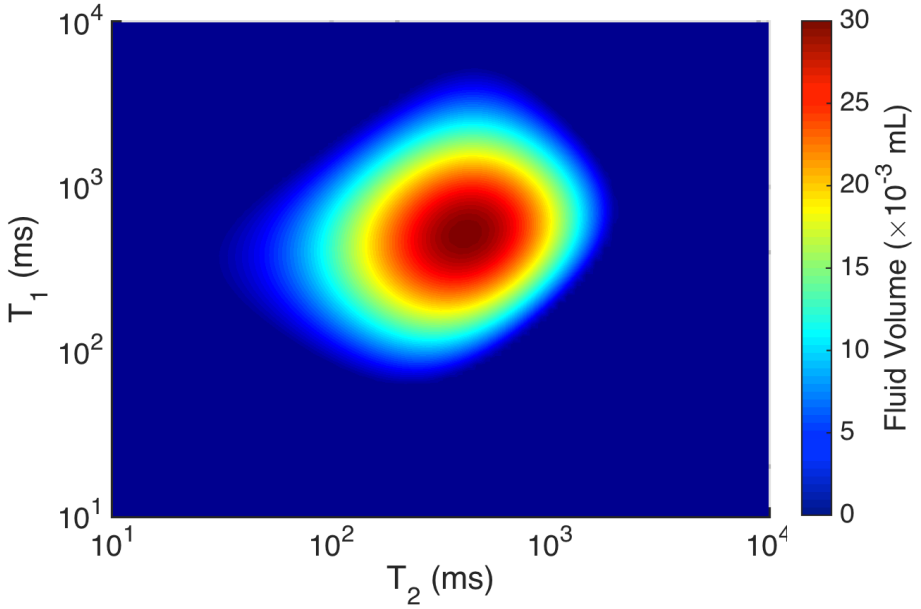

Figure 4.15b: Bead pack (0.25 mm) simultaneous T_1-T_2 NMR map at $\tau = 0.070$ ms.

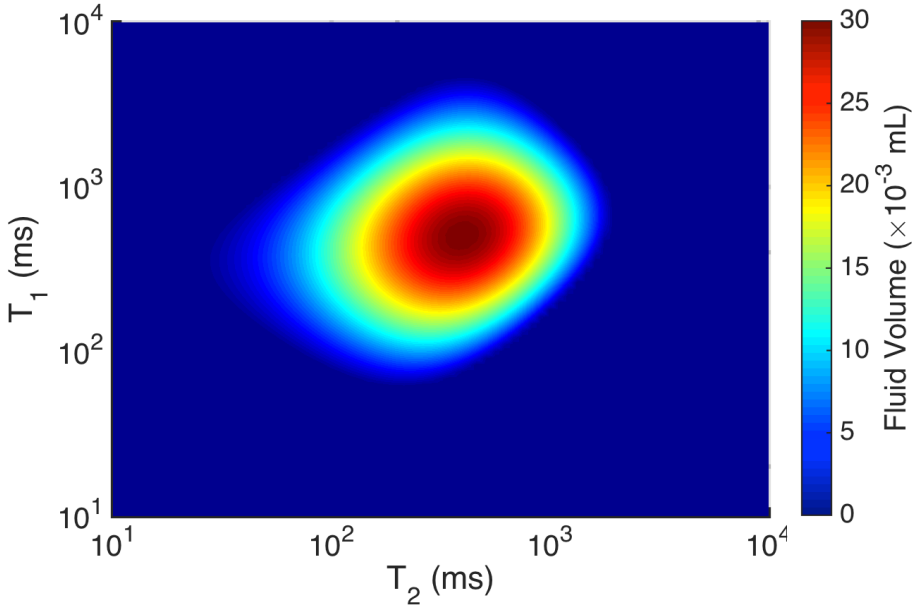

Figure 4.15c: Bead pack (0.25 mm) simultaneous T_1-T_2 NMR map at $\tau = 0.090$ ms.

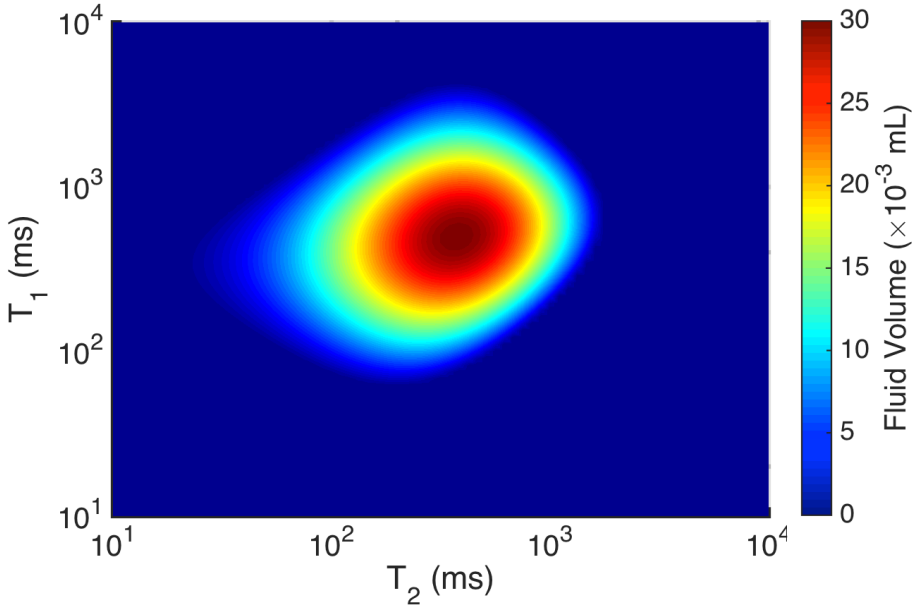

Figure 4.15d: Bead pack (0.25 mm) simultaneous T_1-T_2 NMR map at $\tau = 0.200$ ms.

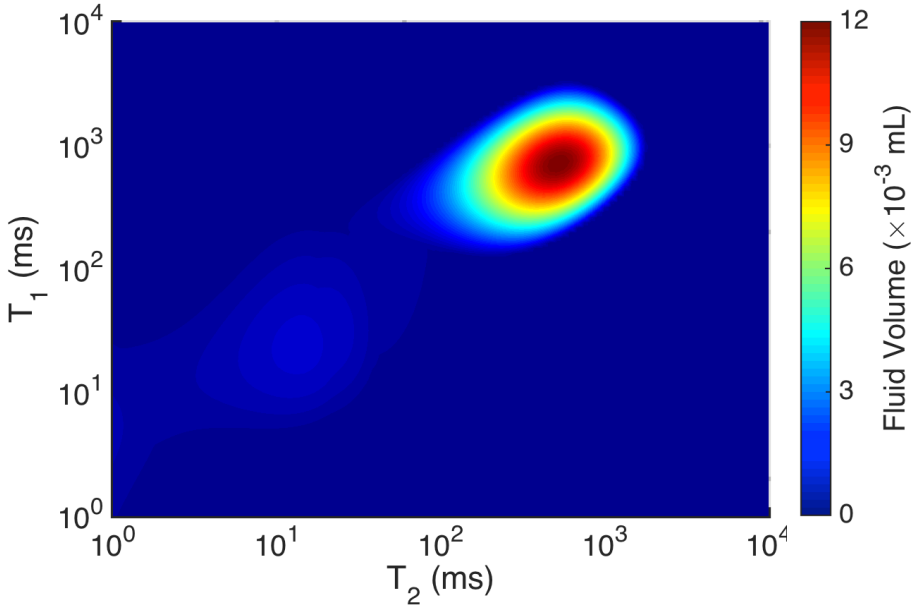

Figure 4.16a: Boise sandstone simultaneous T_1-T_2 NMR map at $\tau = 0.100$ ms.

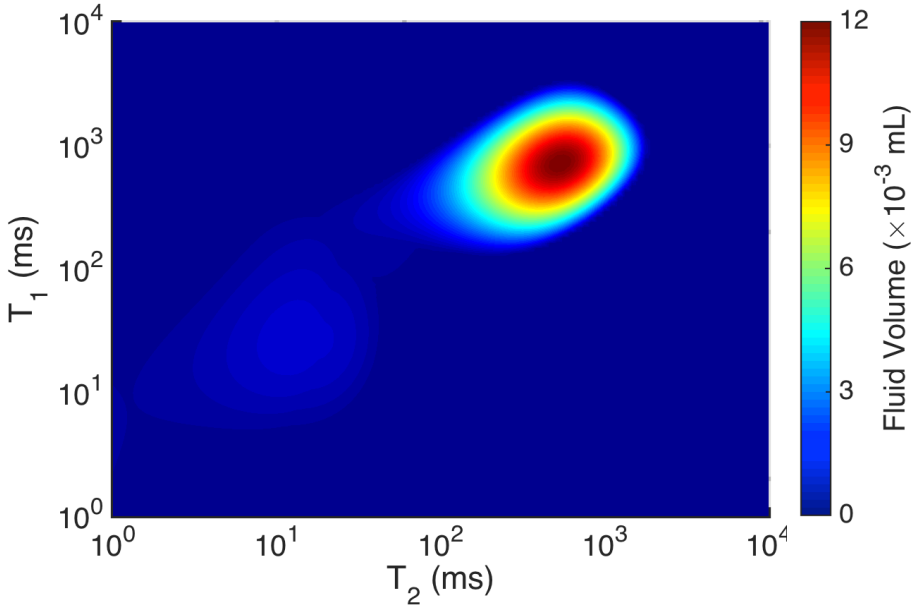

Figure 4.16b: Boise sandstone simultaneous T_1-T_2 NMR map at $\tau = 0.200$ ms.

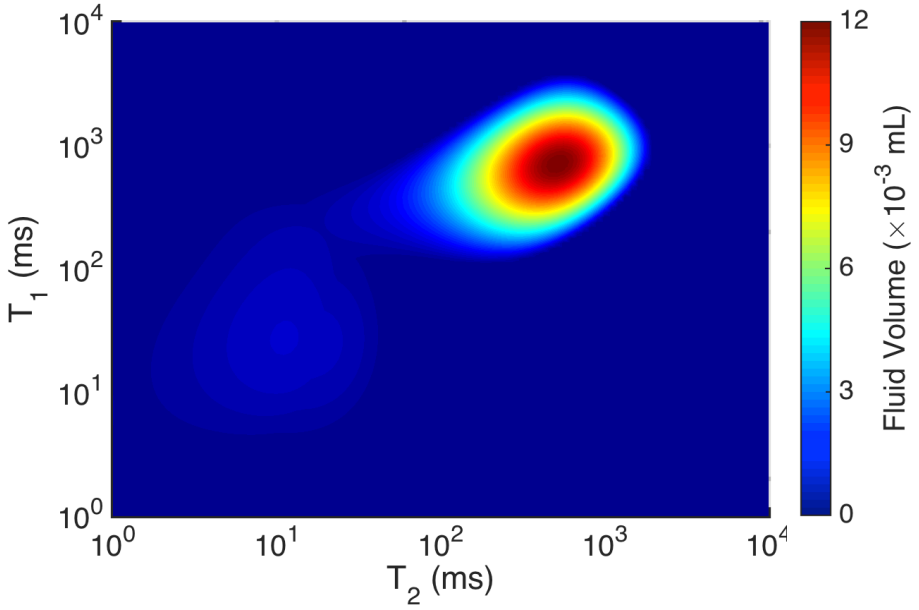

Figure 4.16c: Boise sandstone simultaneous T_1-T_2 NMR map at $\tau = 0.300$ ms.

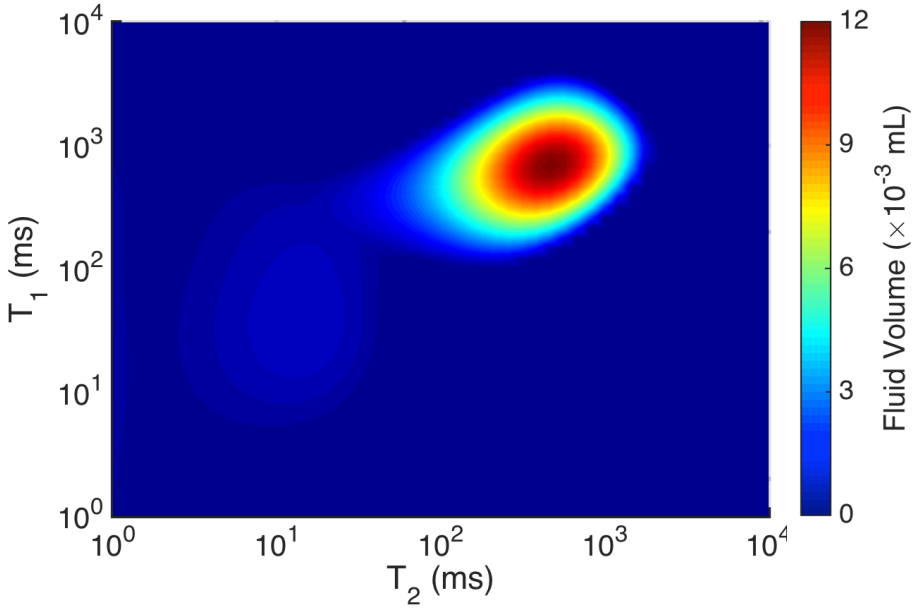

Figure 4.16d: Boise sandstone simultaneous T_1-T_2 NMR map at $\tau = 0.600$ ms.

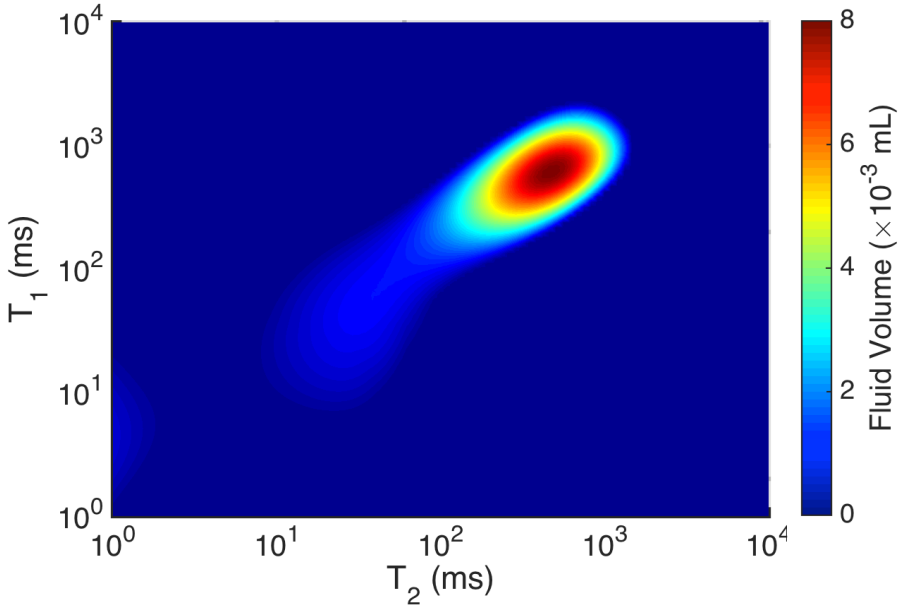

Figure 4.17a: Berea sandstone simultaneous T_1-T_2 NMR map at $\tau = 0.100$ ms.

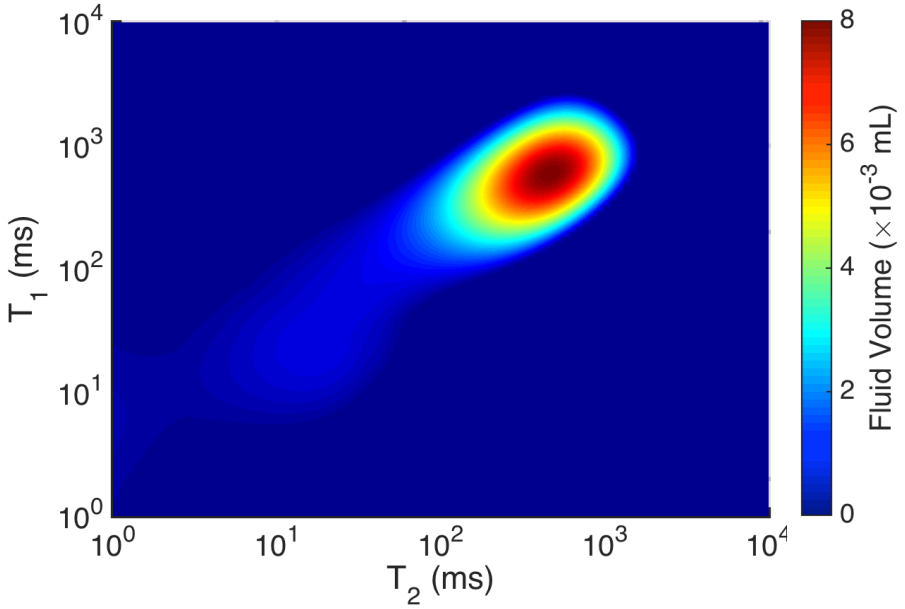

Figure 4.17b: Berea sandstone simultaneous T_1-T_2 NMR map at $\tau = 0.200$ ms.

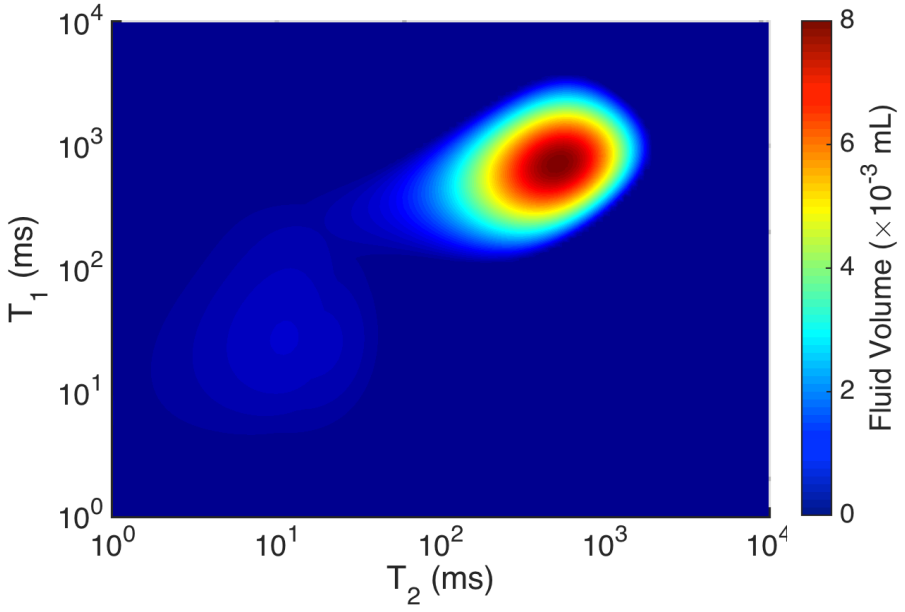

Figure 4.17c: Berea sandstone simultaneous T_1-T_2 NMR map at $\tau = 0.300$ ms.

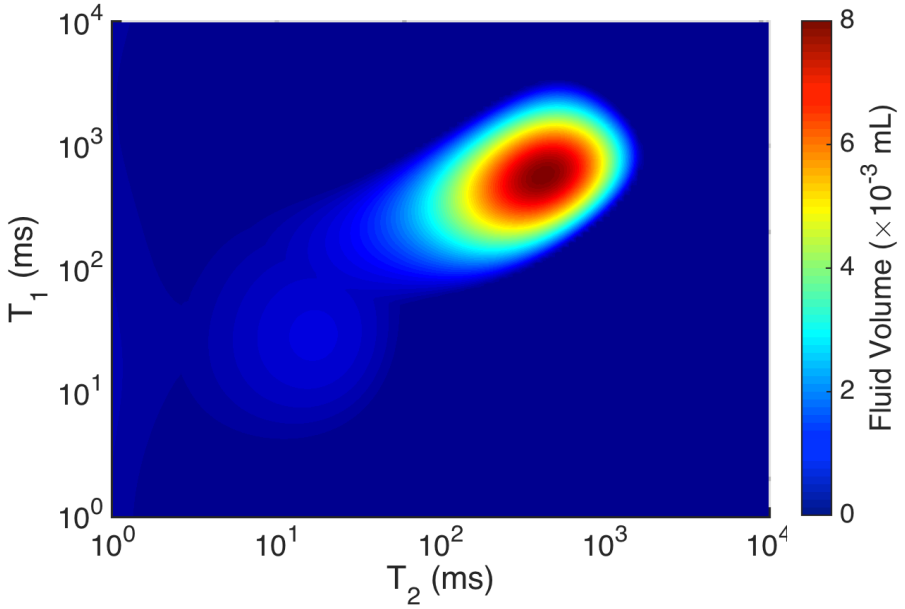

Figure 4.17d: Berea sandstone simultaneous T_1-T_2 NMR map at $\tau = 0.600$ ms.

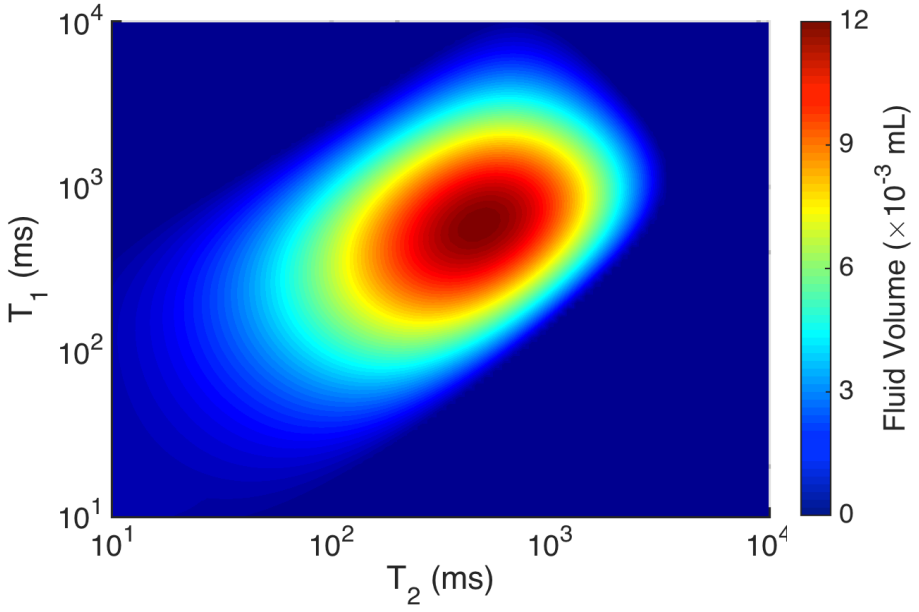

Figure 4.18a: Silurian dolomite simultaneous T_1-T_2 NMR map at $\tau = 0.070$ ms.

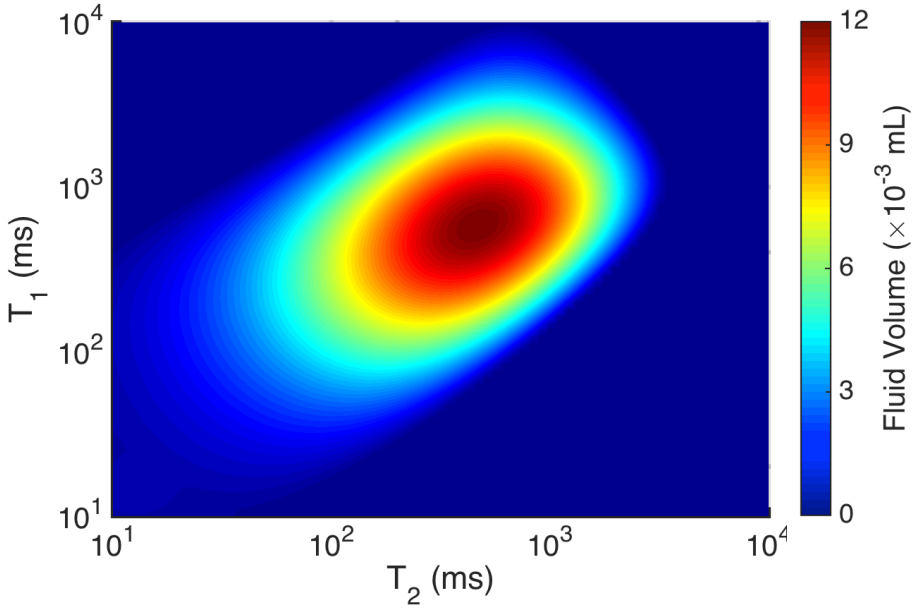

Figure 4.18b: Silurian dolomite simultaneous T_1-T_2 NMR map at $\tau = 0.090$ ms.

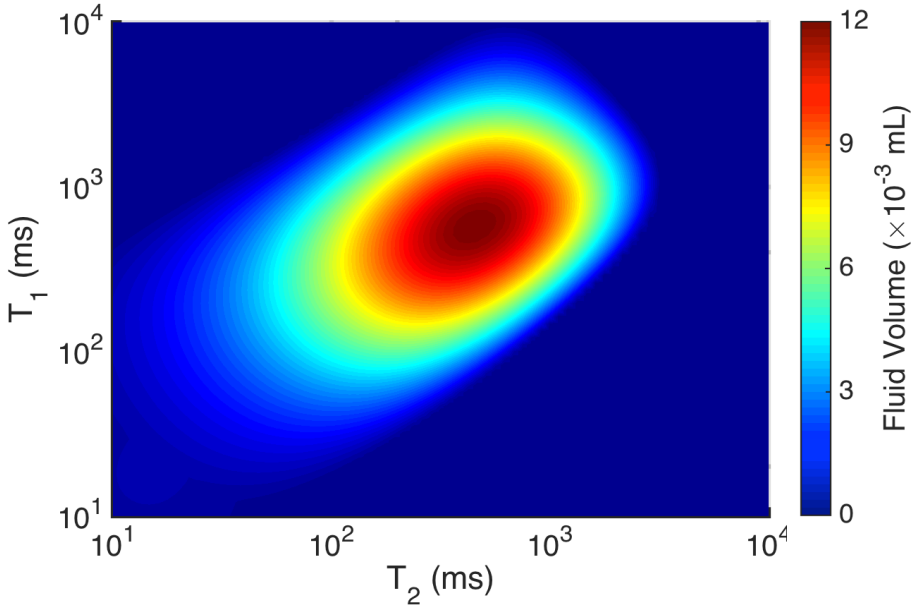

Figure 4.18c: Silurian dolomite simultaneous T_1-T_2 NMR map at $\tau = 0.160$ ms.

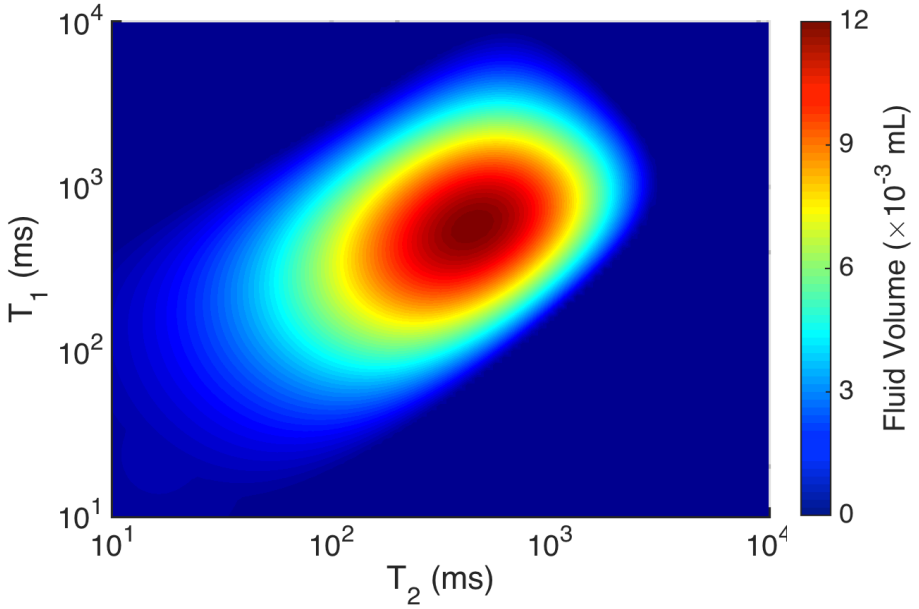

Figure 4.18d: Silurian dolomite simultaneous T_1-T_2 NMR map at $\tau = 0.200$ ms.

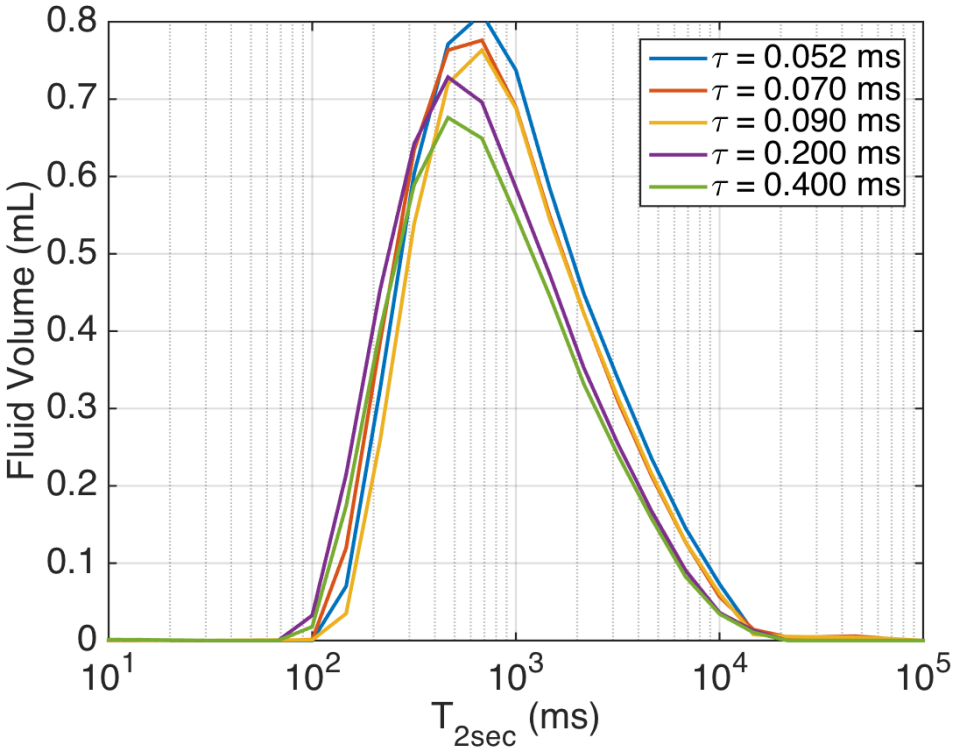

Figure 4.19: Bead pack (0.25 mm) secular relaxation distribution measurements for various CPMG echo half-spacing values.

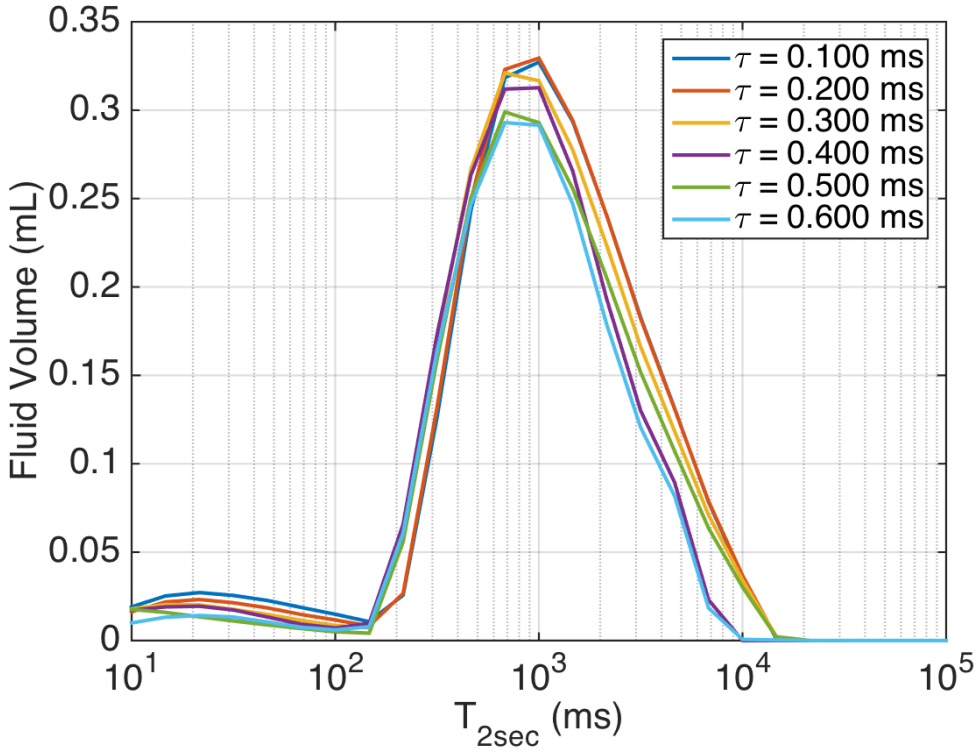

Figure 4.20: Boise sandstone secular relaxation distribution measurements for various CPMG echo half-spacing values.

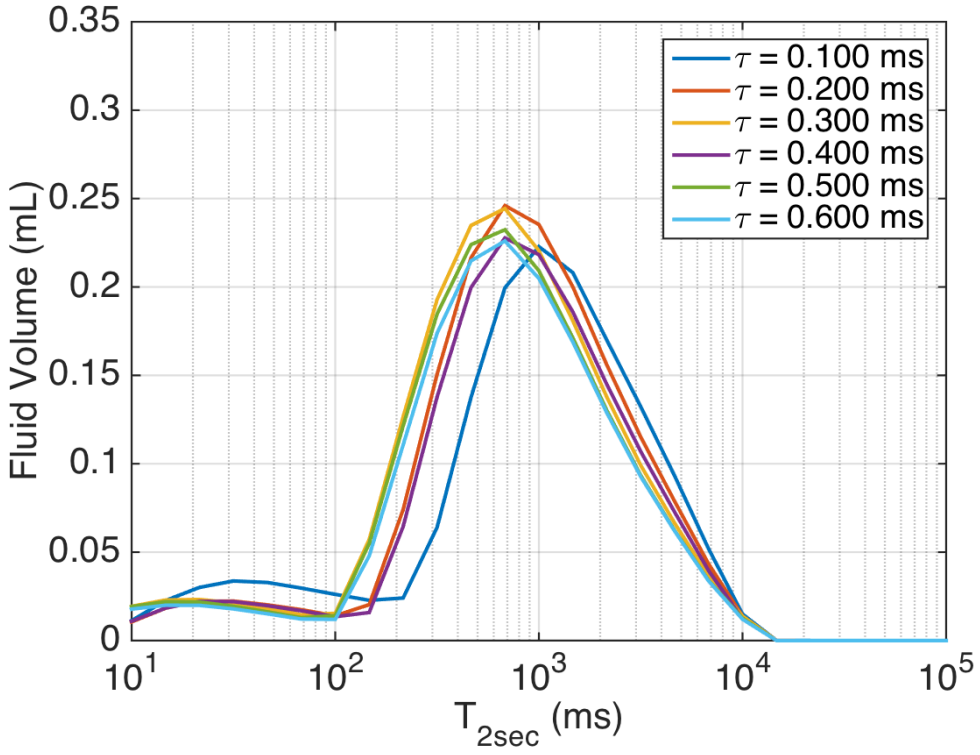

Figure 4.21: Berea sandstone secular relaxation distribution measurements for various CPMG echo half-spacing values.

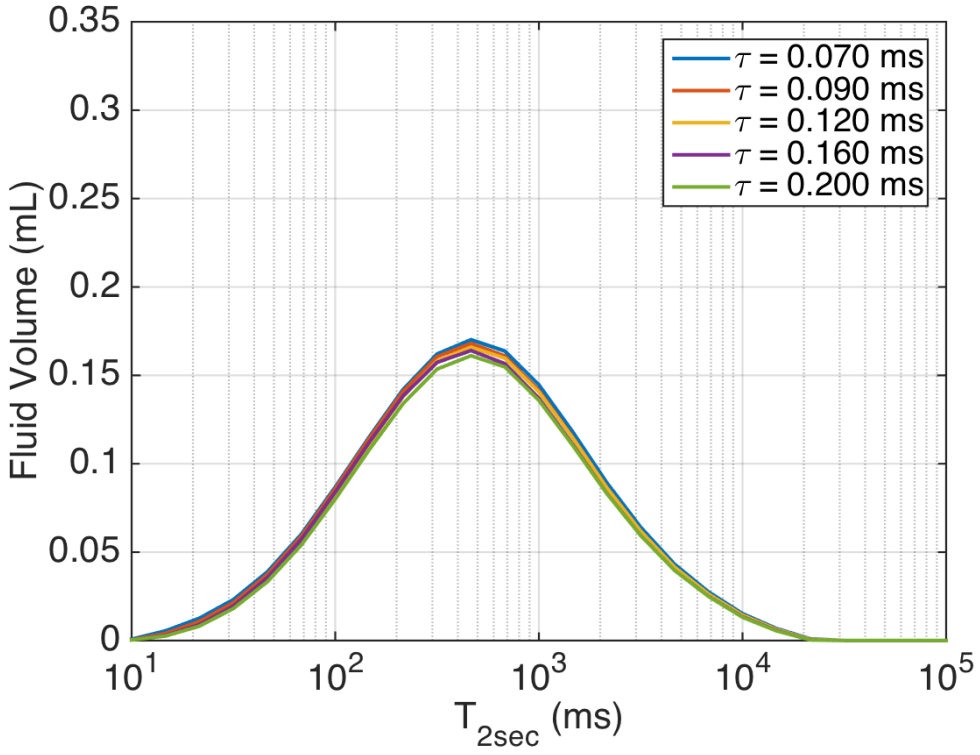

Figure 4.22: Silurian dolomite secular relaxation distribution measurements for various CPMG echo half-spacing values.

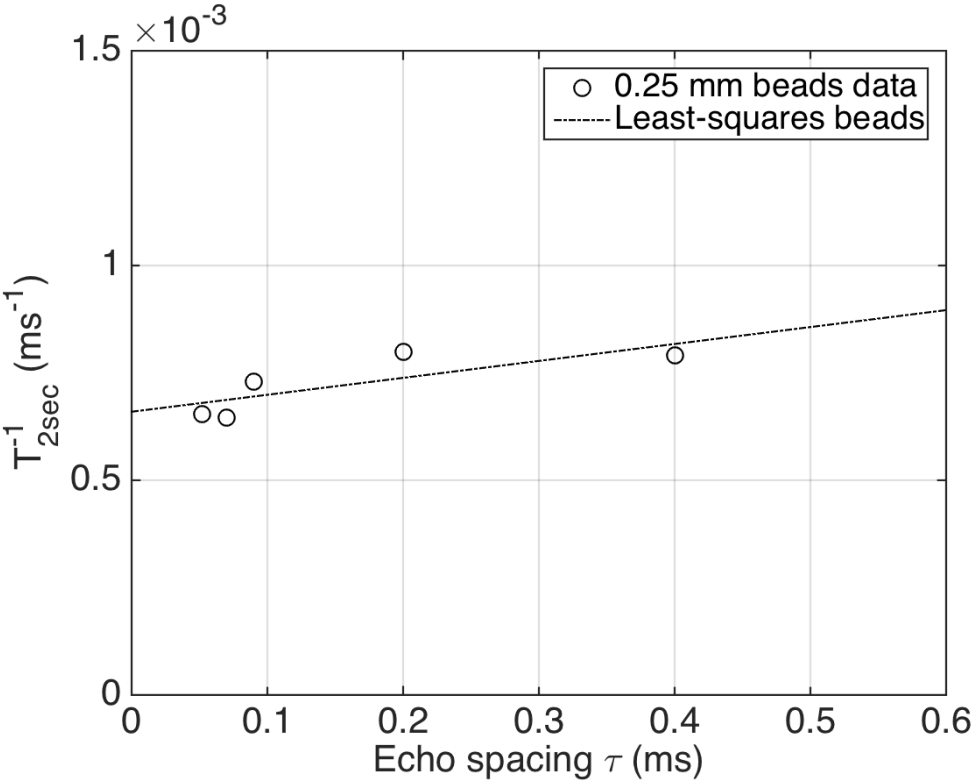

Figure 4.23: Bead pack (0.25 mm) T_{2sec}^{-1} variation with τ; weighted mean measurement data and least squares best fit line. An internal gradient of $G = 0.0466$ T/m was determined by comparing this data to the restricted diffusion model.

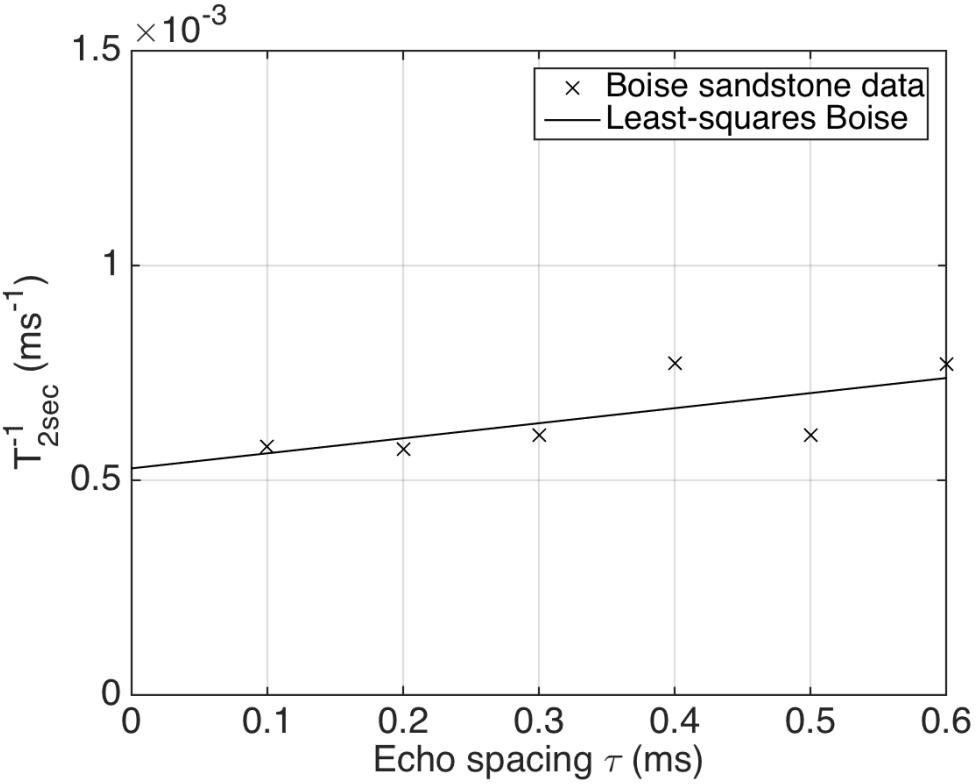

Figure 4.24: Boise sandstone T_{2sec}^{-1} variation with τ; weighted mean measurement data and least squares best fit line. An internal gradient of $G = 0.0671$ T/m was determined by comparing this data to the restricted diffusion model.

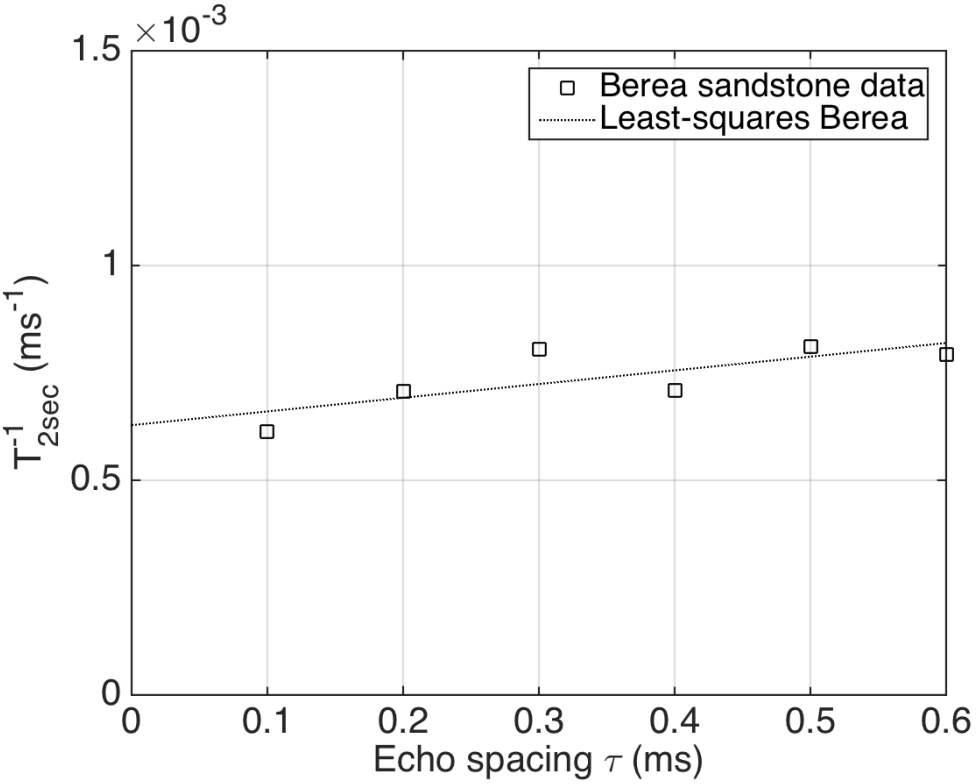

Figure 4.25: Berea sandstone T_{2sec}^{-1} variation with τ; weighted mean measurement data and least squares best fit line. An internal gradient of $G = 0.0644$ T/m was determined by comparing this data to the restricted diffusion model.

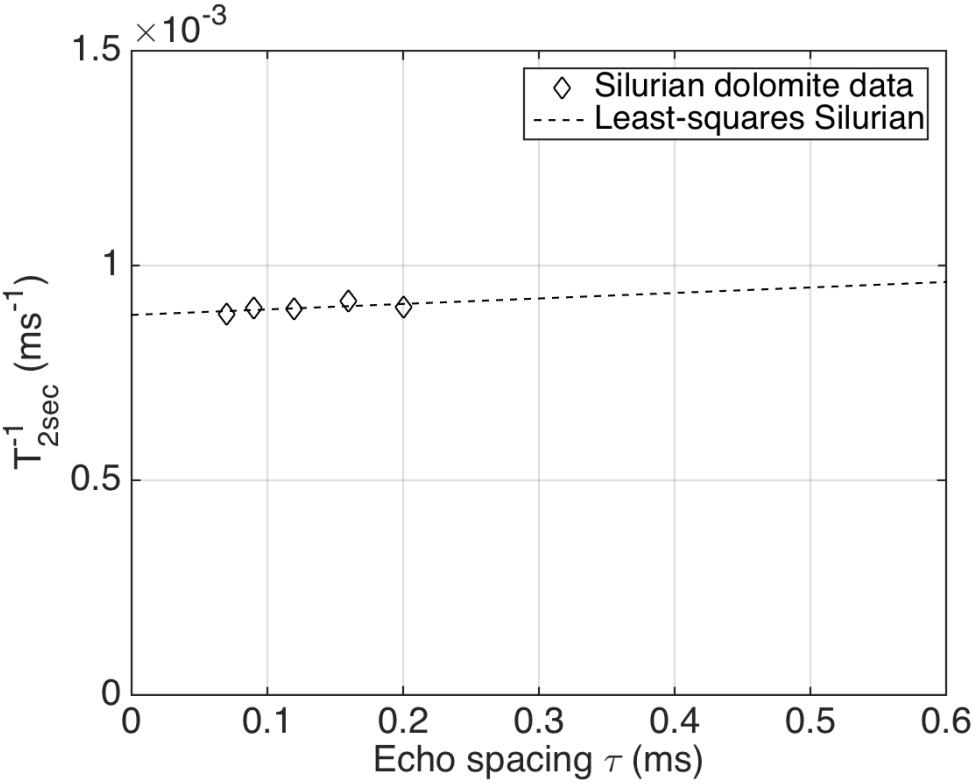

Figure 4.26: Silurian dolomite T_{2sec}^{-1} variation with τ; weighted mean measurement data and least squares best fit line. An internal gradient of $G = 0.0265$ T/m was determined by comparing this data to the restricted diffusion model.

4.3.2 Pore Size Optimization

A parameter space defined by pore radius (R) and the difference in transverse and longitudinal surface relaxivities ($\Delta\rho = \rho_2 - \rho_1$) was tested as input to the restricted diffusion model and compared with variation in secular relaxation data. Goodness of fit χ^2 was calculated for each R-$\Delta\rho$ pair (Figures 4.27a, 4.28a, 4.29a, and 4.30a). The χ^2 map for each sample exhibits a best-fit path along a sloped line in R-$\Delta\rho$ space. To better visualize the behavior of χ^2 along this path, the minimum χ^2 value in the $\Delta\rho$ dimension was selected at each R and plotted in Figures 4.27b, 4.28b, 4.29b, and 4.30b. Each plot effectively displays the behavior of χ^2 in the "trough" of each χ^2 map and elucidates any convergence to a minimum, if one should exist. Flattening of the χ^2 map into the R-dimension and $\Delta\rho$ dimension are also shown in Figures 4.27c-d, 4.28c-d, 4.29c-d, and 4.30c-d, flattened along the planes of best-fit $\Delta\rho$ and R values, respectively.

Gaussian white noise was introduced to the model at both 5% and 10% standard deviation to probe the sensitivity of the model. Significant variation in results, particularly with the introduction of just 5% standard deviation noise, indicates solution instability. The χ^2 analysis appears to converge stably for the sample of Boise sandstone at both noise levels. Best-fit values of R = 3.44 μm and $\Delta\rho$ = 0.64 μm/s were extracted. However, despite the stability of these solutions, their values fall short of expected typical values (i.e. R = 145 μm; $\Delta\rho \sim$ O(10 μm/s)). The results for Berea sandstone, R = 3.62 μm and $\Delta\rho$ = 0.79 μm/s, are stable at 5% standard deviation, but not 10% standard deviation. These results are also much smaller than what is expected for Berea sandstone (i.e. R = 41.4 μm; $\Delta\rho$ = 23.2 μm/s). The samples of Silurian dolomite and the 0.25 mm bead pack are demonstrably unstable, even with the introduction of just 5% standard deviation noise. For samples such as these, where pore sizes are expected to be quite large (i.e. R = 173.1 μm for Silurian dolomite; $R \sim$ 125 μm for the bead pack),

sensitivity of the restricted diffusion model as a function of pore size is expected to be quite small. Figure 4.31 plots the restricted diffusion model explicitly as a function of pore size for an internal gradient of $G = 0.0466$ T/m as determined for the bead pack from the previous analysis. Note that $1/T_{2D}$ becomes very weakly sensitive to R as R increases. This is a likely cause of the inability of the χ^2 analysis to converge on a stable best-fit parameter pair solution. Figure 4.29a indicates a multiplicity of solutions for Silurian dolomite along a sloped R-$\Delta\rho$ path that is confirmed by Figure 4.29b. This corroborates the conclusion that $1/T_{2D}$ is weakly sensitive to R, since with a negligible $1/T_{2D}$ term, modeled secular relaxation becomes

$$T_{2sec,mod,i} = \left(\frac{3(\rho_2 - \rho_1)}{R} + \frac{1}{T_{2D}(\tau_i, R)}\right)^{-1} \approx \frac{R}{3(\rho_2 - \rho_1)}$$

which is decidedly unstable when optimized for R and $\Delta\rho$. A similar situation arises for the large-pored bead pack, where the multiplicity of solutions exhibited in Figures 4.30a and 4.30b arises due to insensitivity of $1/T_{2D}$ to pore size at the relevant scale. A potential way of correcting this is to investigate model behavior for a different range of echo half-spacing values. Figure 4.32 shows the model evaluated for much larger τ. Note that $1/T_{2D}$ is more sensitive to changes in radius, even at larger radii. This may offer a method of stabilizing the optimization for samples with larger mean pore sizes.

Another issue with the optimization is highlighted by the results for Berea and Boise sandstones. The sample of Berea sandstone appears to have solutions that are stable to 0.05σ and the sample of Boise sandstone stable to 0.10σ. However, the converged values are unexpectedly small for these samples (**S4.2**; Krohn 1998). A likely cause of this is that the internal magnetic field gradients present in the samples are too weak, and

the number of data points in τ too few, to provide sufficiently accurate and precise determination of internal magnetic field gradients. Then, when used as input to the model for determination of pore sizes, gradients perturb the solutions for the sandstones away from reasonable expected values. In other words, gradients must be known to high accuracy when input to the model to correctly extract pore size. This effect becomes even more pronounced with lessened R sensitivity at larger pore sizes. A greater number of τ-varied measurements may be run, particularly for samples with expectedly large internal magnetic field gradients, to test this hypothesis. Gradients in samples with strongly magnetic species, characterized by a larger number of data points, might then be determined sensitively enough to properly invert for pore size.

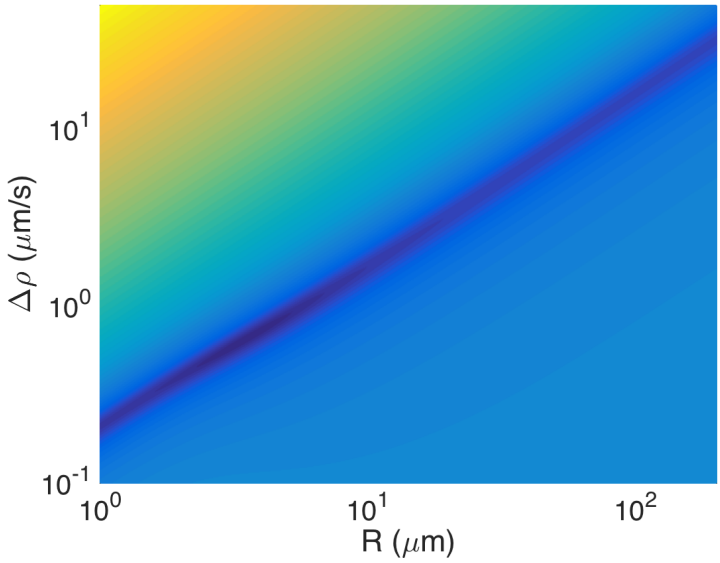

Figure 4.27a: Boise sandstone parameter space χ^2 for R and $\Delta\rho$. Darker blue shades represents smaller values of χ^2.

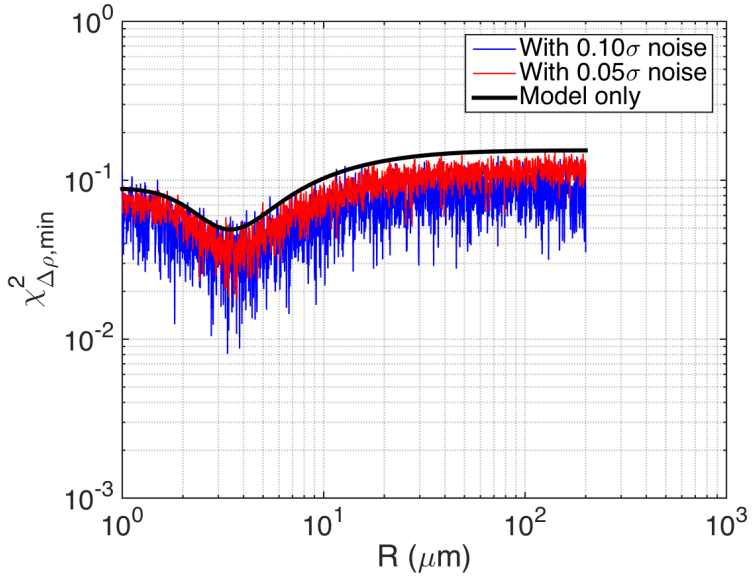

Figure 4.27b: Boise sandstone χ^2 traced along the trough of minimum χ^2 in the $\Delta\rho$ dimension at each R value. Gaussian white noise has been added to the model.

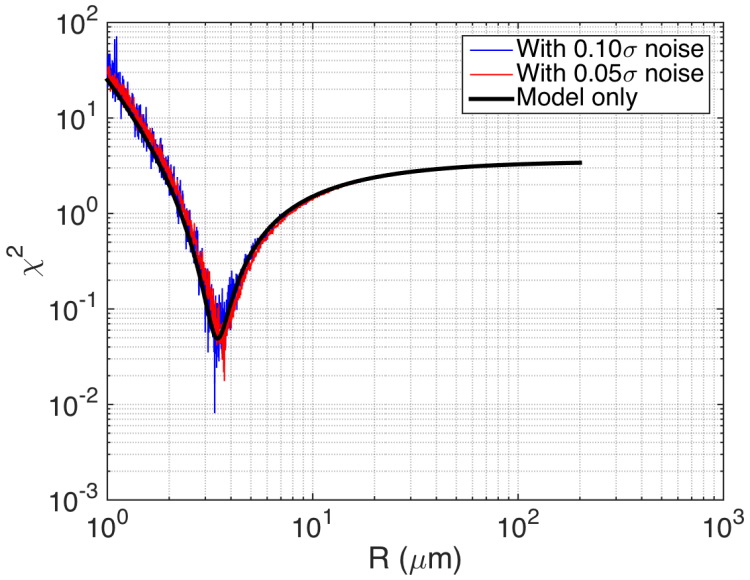

Figure 4.27c: Boise sandstone χ^2 for R in the plane of best-fit $\Delta\rho$.

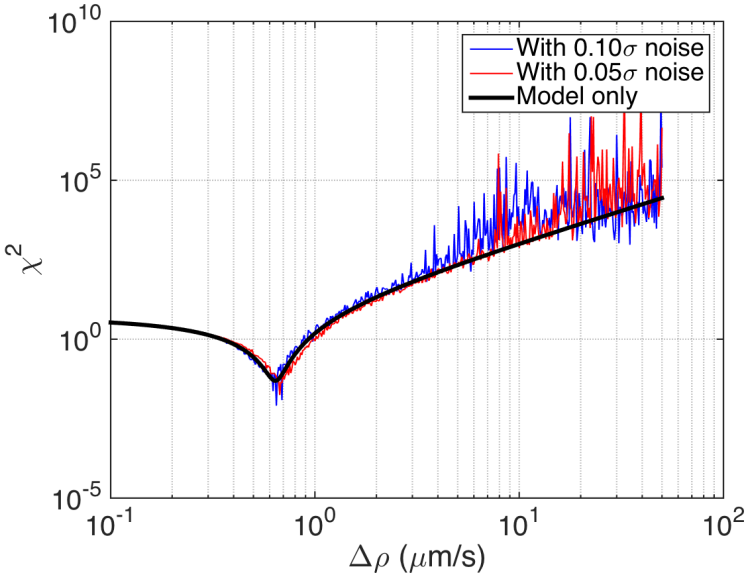

Figure 4.27d: Boise sandstone χ^2 for $\Delta\rho$ in the plane of best-fit R.

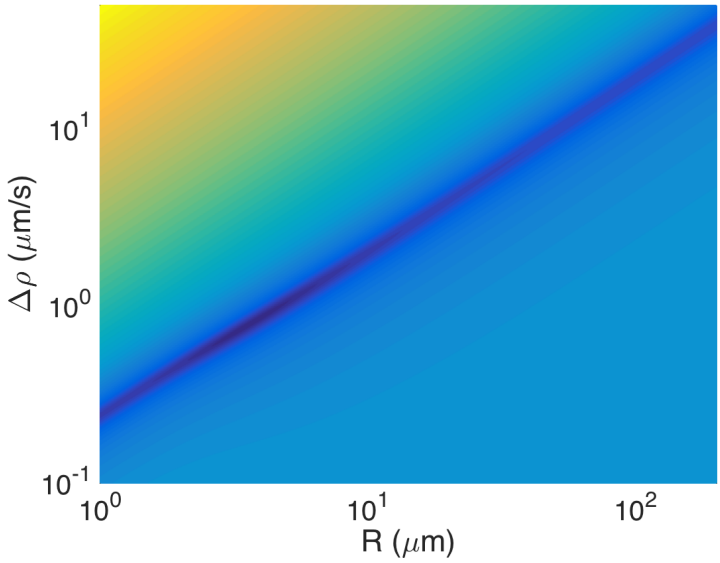

Figure 4.28a: Berea sandstone parameter space χ^2 for R and $\Delta\rho$. Darker blue shades represents smaller values of χ^2.

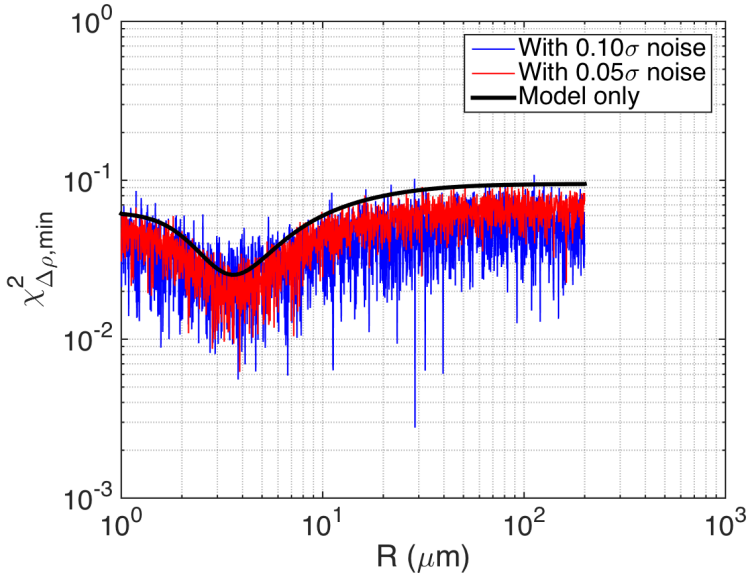

Figure 4.28b: Berea sandstone χ^2 traced along the trough of minimum χ^2 at each R value. Gaussian white noise has been added to the model to test optimization sensitivity.

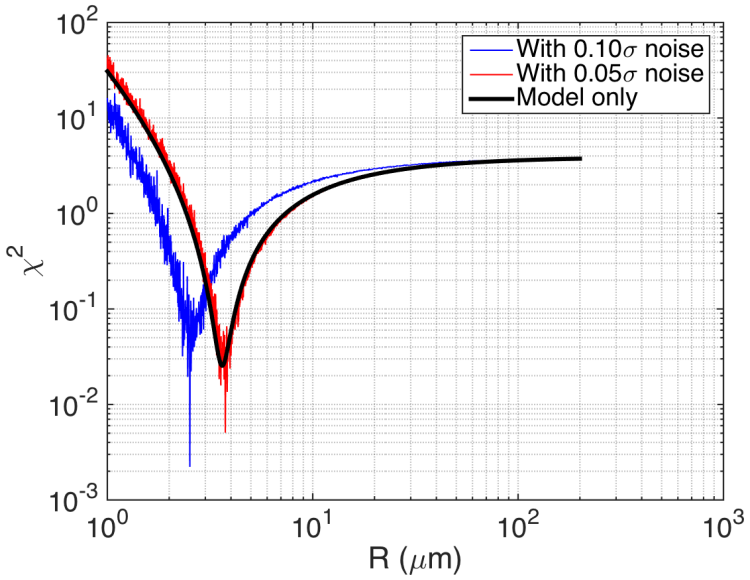

Figure 4.28c: Berea sandstone χ^2 for R in the plane of best-fit $\Delta\rho$.

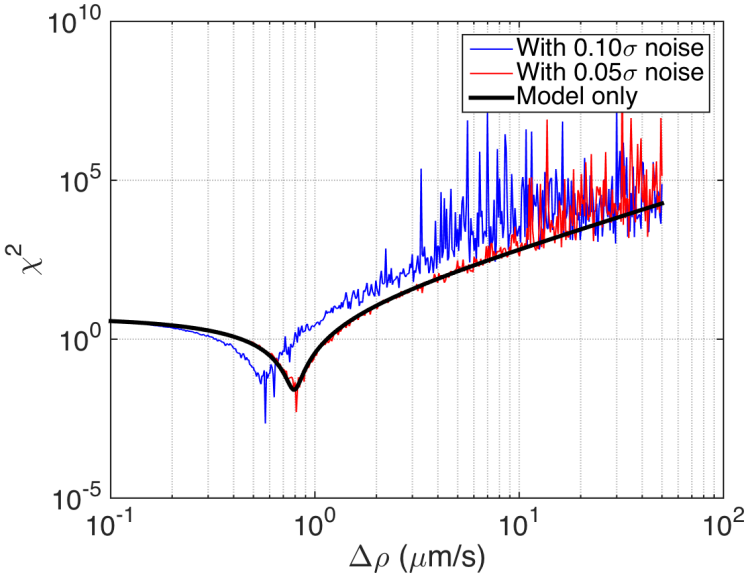

Figure 4.28d: Berea sandstone χ^2 for $\Delta\rho$ in the plane of best-fit R.

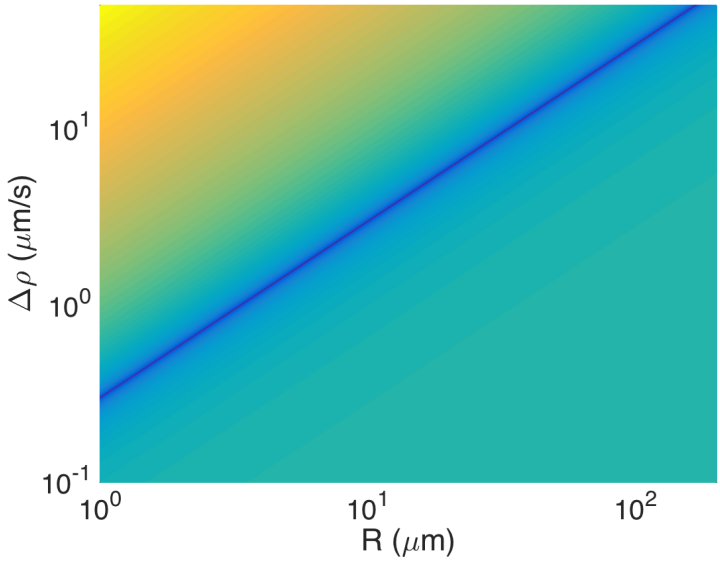

Figure 4.29a: Silurian dolomite parameter space χ^2 for R and $\Delta\rho$. Darker blue shades represents smaller values of χ^2.

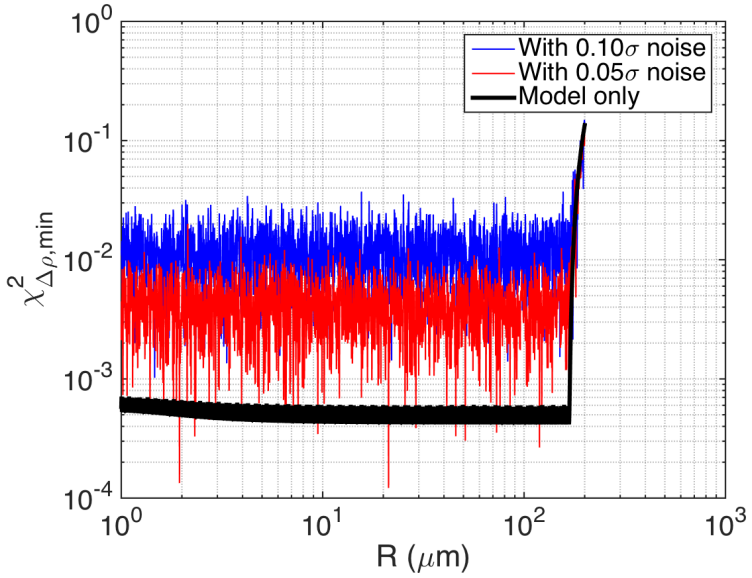

Figure 4.29b: Silurian dolomite χ^2 traced along the trough of minimum χ^2 at each R value. Gaussian white noise has been added to the model to test optimization sensitivity.

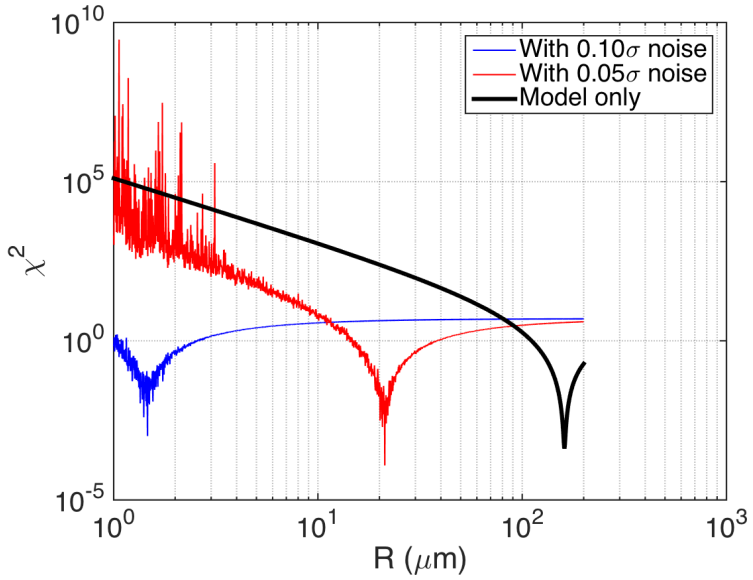

Figure 4.29c: Silurian dolomite χ^2 for R in the plane of best-fit $\Delta\rho$.

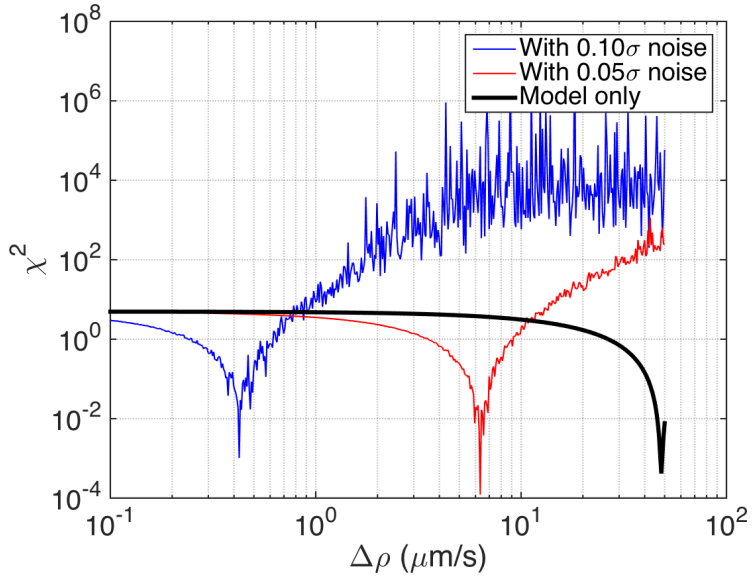

Figure 4.29d: Silurian dolomite χ^2 for $\Delta\rho$ in the plane of best-fit R.

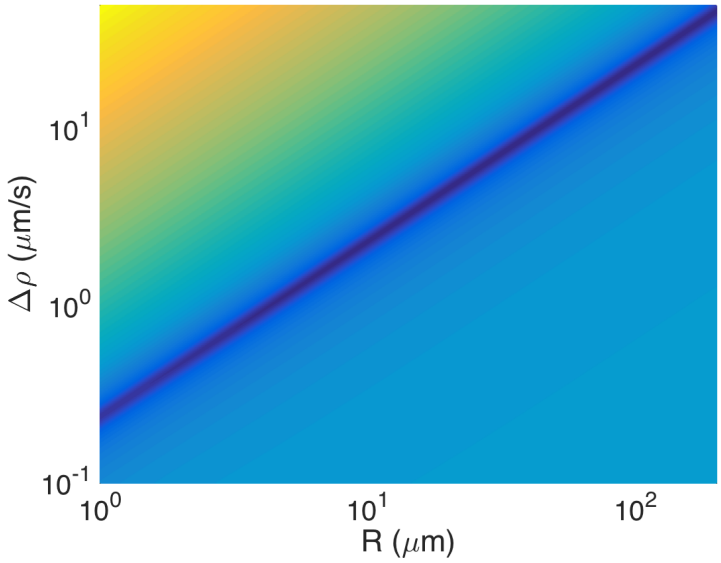

Figure 4.30a: Bead pack parameter space χ^2 for R and $\Delta\rho$. Darker blue shades represents smaller values of χ^2.

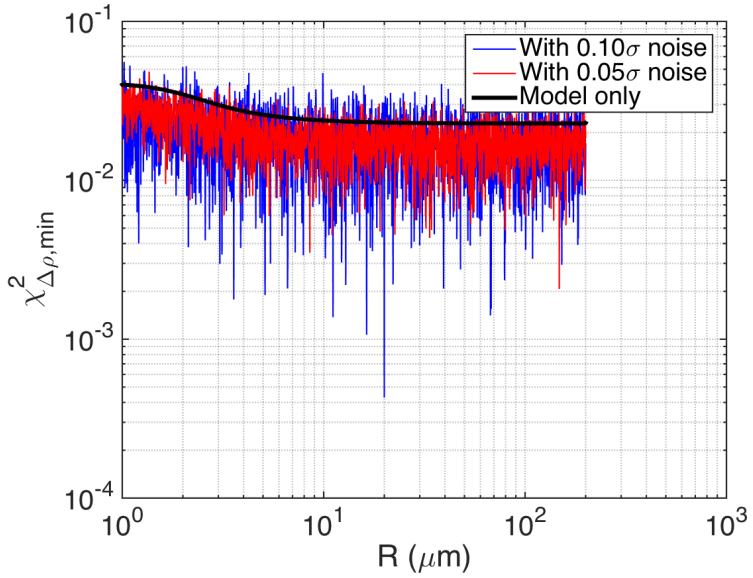

Figure 4.30b: Bead pack χ^2 traced along the trough of minimum χ^2 at each R value. Gaussian white noise has been added to the model to test optimization sensitivity.

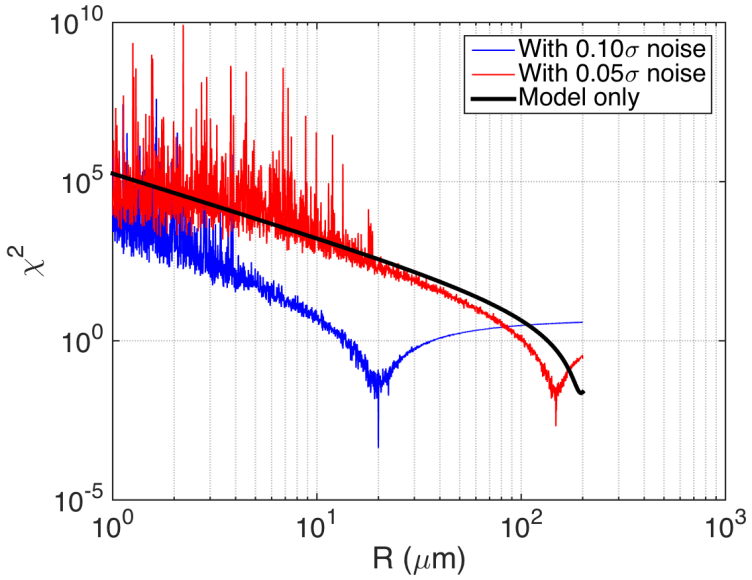

Figure 4.30c: Bead pack χ^2 for R in the plane of best-fit $\Delta\rho$.

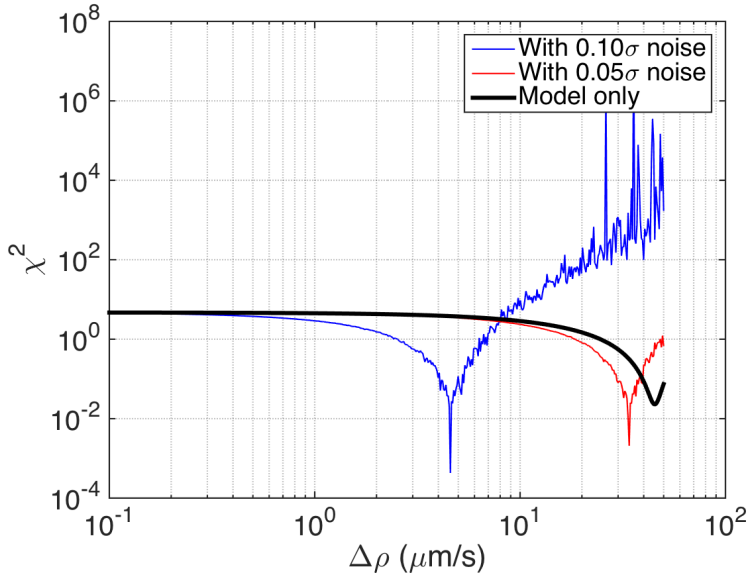

Figure 4.30d: Bead pack χ^2 for $\Delta\rho$ in the plane of best-fit R.

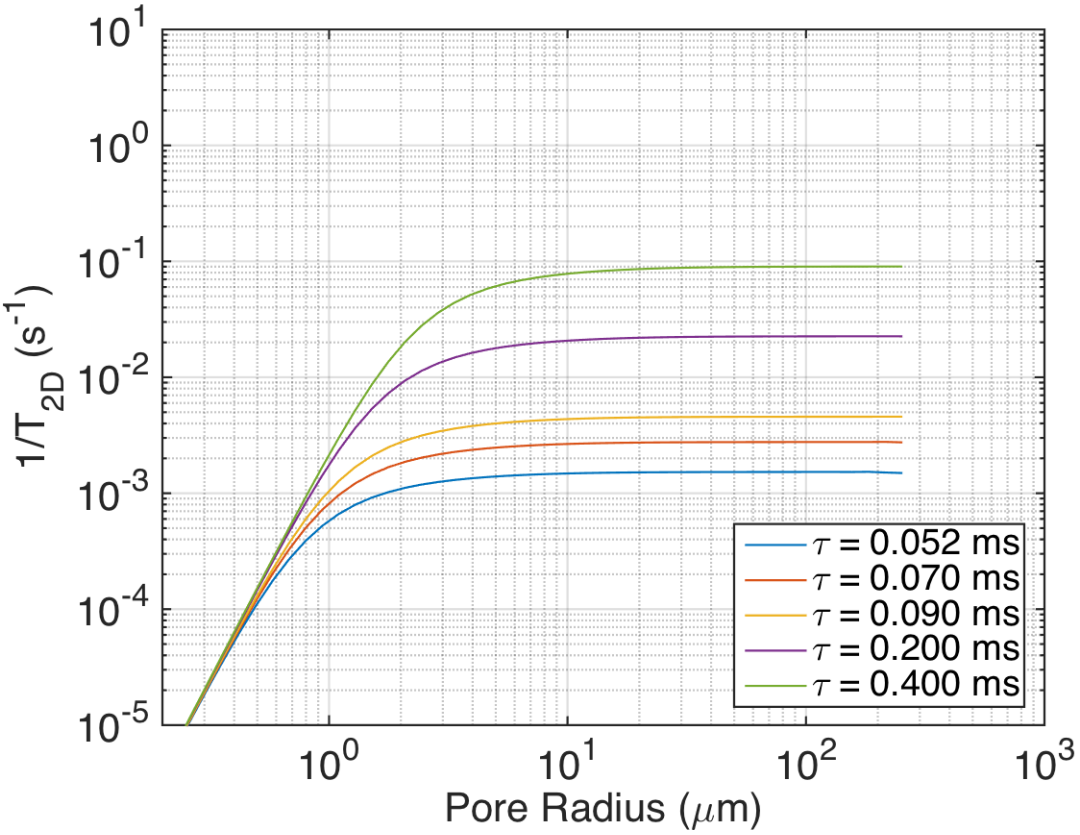

Figure 4.31: Neuman's restricted diffusion model for diffusion relaxation rate as a function of pore radius. Note that $1/T_{2D}$ becomes increasingly insensitive to changes in pore radius as pore radius increases.

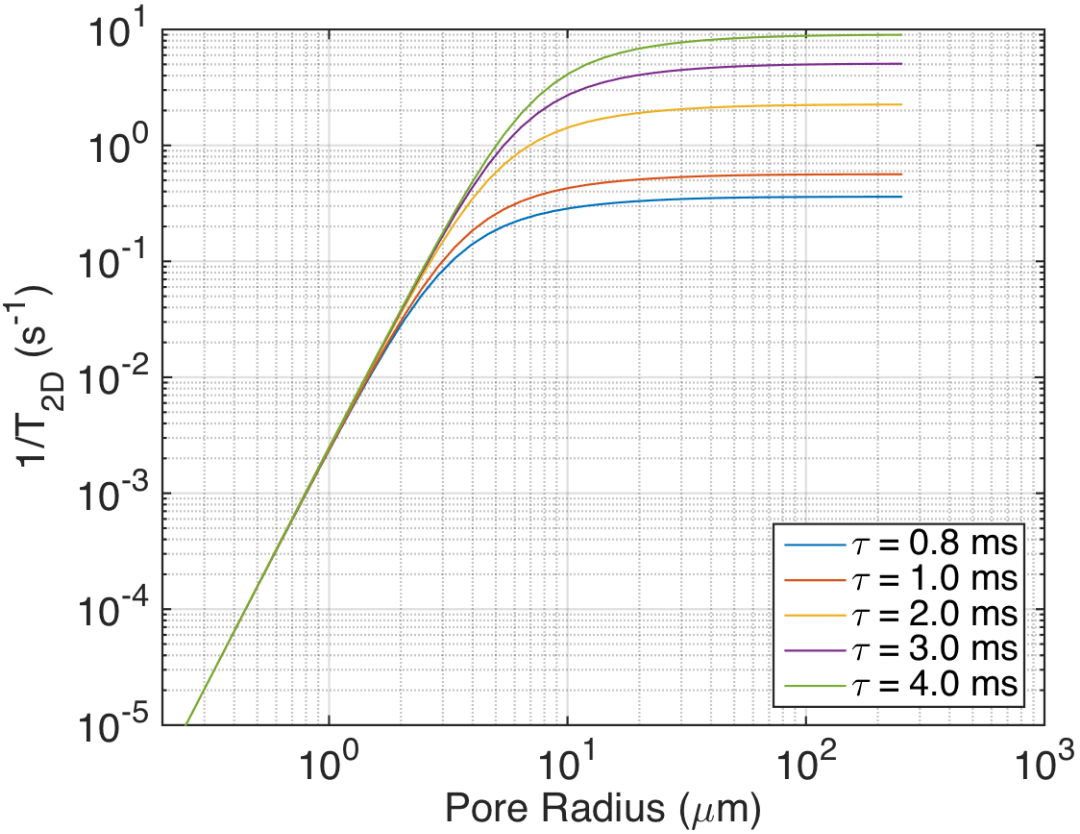

Figure 4.32: Neuman's restricted diffusion model for diffusion relaxation rate as a function of pore radius. Large echo half-spacing values are used in the model. Note that inverse diffusion relaxation is more sensitive as a function of echo spacing, even for larger values of radius. This may offer a means to stabilize inversions for samples with large mean pore sizes.

4.3.3 Ideas for Future Work

Image Analysis: Results obtained via image analysis could be improved by increasing the working-volumes of the analyzed three-dimensional image stacks. Because 3DMA-rock is computationally intensive, sub-volumes of the full three-dimensionally images were cleaned, binarized, and analyzed for extraction of pore-throat networks and pore size distributions. Additionally, in the extraction of pore radii from 3DMA pore throat networks, pores were assumed spherical. The 3DMA-rock software allows for direct extraction of surface-to-volume ratios for pores, however, which would be more accurate in correlation with NMR measurements.

NMR Experiments: In the continuation of this study, it would be useful to obtain measurements with a greater number of echo half-spacing values for a given sample. These values should be as large as possible while permitting for sufficiently dense T_1 sampling. This will allow for extraction of pore sizes for samples with large pore sizes, since a larger echo spacing range is more sensitive to variation in radius even at large radii. In addition, to ensure that gradients are characterized with sufficient accuracy and precision, only samples with large expected internal magnetic field gradients should be analyzed. This should ensure that gradients to be input to the $R - \Delta\rho$ optimization are ascertained well enough that converged values are meaningful. Otherwise, a small change in gradient may greatly affect the value of a converged pore size. This may resolve the issue that internal gradients were too small to be sufficiently characterized by so few data points.

The redundancy present in the secular relaxation analyses (i.e., gradients obtained using known pore sizes in the first analysis were used as input in the model in the second analysis) may present a confirmation of accurate determination of pore sizes and gradients after the aforementioned steps are imposed to correct the process. In such a

case, in which confirmation of the method's integrity is established, a non-circular analysis may be performed. The proof-of-concept in the two-step method presented here can be used to ensure that a sufficient number of data points and sufficiently large gradients and echo half-spacing values are used to analyze the pore system using the restricted diffusion model. A next step might be to simultaneously extract pore sizes, internal magnetic field gradients, and the differences in surface relaxivities using, for example, a non-linear least squares analysis.

Fluid effects: An avenue of interest may be in the effect on the secular relaxation response of partial saturation of brine-saturated rocks with light mineral oil. The expectation would be that secular relaxation should remove the effect of fluids from the NMR distribution, since longitudinal and transverse bulk relaxation times should be similar enough to cancel each other's contribution. This would allow an analysis of the sort presented in this thesis, where the effect of diffusion could be isolated, free from the complications brought on by multiple saturating phases. Preliminary results, however, show unaccounted for behavior in the presence of light oil and brine. An investigation of this behavior may prove yet predictable and a fluid-independent secular relaxation analysis therefore feasible. The benefit of such an analysis would be extraction pore size, gradient, and surface relaxivity information direcly from NMR data, independently of multiple saturating phases.

References

Alley, M., & Korosec, F.R. (2009). MR physics and techniques for clinicians. [Course notes]. Retrieved from http://afni.nimh.nih.gov/sscc/staff/rwcox/ISMRM_2006/ISMRM%20M-F%202006/files/TuE_01.pdf

Arns, C. H. (2004). A comparison of pore size distributions derived by NMR and X-ray-CT techniques. *Physica A: Statistical Mechanics and Its Applications*, *339*(1-2), 159–165. http://doi.org/10.1016/j.physa.2004.03.033

Anand, V., & Hirasaki, G. (2008). Paramagnetic Relaxation in Sandstones: Distinguishing T1 and T2 Dependence on Surface Relaxation, Internal Gradients and Dependence on Echo Spacing. *Fluid-Rock Characterization for NMR Well Logging*. *190*(1), 68–85. http://doi.org/10.1016/j.jmr.2007.09.019

Bloch, F. (1951). Nuclear relaxation in gases by surface catalysis. *Physical Review*, *83*(5), 1062–1063. http://doi.org/10.1103/PhysRev.83.1062

Brownstein, K. R., & Tarr, C. E. (1979). Importance of classical diffusion in NMR studies of water in biological cells. *Physical Review A*, *19*(6), 2446–2453.

Canet, D., Levy, G. C., & Peat, I. R. (1975). Time saving in 13C spin-lattice relaxation measurements by inversion-recovery. *Journal of Magnetic Resonance*, *18*(1), 199-204. http://doi.org/10.1016/0022-2364(75)90238-3

Carr, H. Y., & Purcell, E. M. (1954). Effects of diffusion on free precession in nuclear magnetic resonance experiments. *Physical Review, 94*(3), 630-638. http://doi.org/10.1103/PhysRev.94.630

Coates, G.R., et al. (1991, June 16-19). *The MRIL in Conoco 33-1—an investigation of a new magnetic resonance imaging log*. Paper presented at 32nd Annual SPWLA Logging Symposium.

Coates, George R., Lizhi Xiao, & Manfred G. Prammer. *NMR Logging: Principles and Applications*. Houston: Haliburton Energy Services, 1999. Print.

Daigle, H., Johnson, A., & Thomas, B., (2014). Determining fractal dimension from NMR data in rocks with internal magnetic field gradients, *Geophysics,* 79(6), D425-D431. http://dx.doi.org/10.1190/GEO2014-0325.1.

Daigle, H., Thomas, B., Rowe, H., & Nieto, M. (2014). Nuclear magnetic resonance characterization of shallow marine sediments from the Nankai Trough, Integrated Ocean Drilling Program Expedition 333. *Journal of Geophysical Research: Solid Earth*, *119*(4), 2631-2650. http://doi.org/10.1002/2013JB010784

Dunn, K. J., Latorraca, G. A., Warner, J. L., & Bergman, D. J., (1994, September 25-28). *On the calculation and interpretation of NMR relaxation time distributions*. Paper presented at the 69th Annual Technical Conference of the SPE.

Erb, E., & Uebersfeld, J. (1958). An apparatus magnetic double resonance application to carbon. *Comptes Rendus Physique*, *246*, 2121.

Garwin, R. L., & Reich, H. A. (1959). Self-diffusion and nuclear relaxation in He-3. *Physical Review*. *115*(6), 1478-1492. http://dx.doi.org/10.1103/PhysRev.115.1478

Gillis, P., & Koenig, S. (1987). Transverse relaxation of solvent protons induced by magnetized spheres: application to ferritin, erythrocytes, and magnetite. *Magnetic Resonance in Medicine*, *5*(4), 323–345. http://onlinelibrary.wiley.com/doi/10.1002/mrm.1910050404/abstract

Hahn, E. (1950). Spin Echoes. *Physical Review*, *80*(4), 580–594. http://doi.org/10.1103/PhysRev.80.580

Jones, D. E. (1972). Fourier transform nuclear magnetic resonance III spin-lattice relaxation times. *Journal of Magnetic Resonance*, *6*(2)**,** 191-196. doi:10.1016/0022-2364(72)90126-6

Katz, A. J., & Thompson A. H. (1987). Prediction of rock electrical conductivity from mercury injection measurements. *Journal of Geophysical Research, 92*(B1), 599-607, doi:10.1029/jb092ib01p00599.

Kleinberg, R. L. (1999). Nuclear Magnetic Resonance. In C. L. Tang (Ed.), *Experimental Methods in the Physical Sciences,* (15).

Kleinberg, R. L., & Horsfield, M. (1989). Transverse relaxation processes in porous sedimentary rock. *Journal of Magnetic Resonance*, *88*(1), 9–19. http://doi.org/10.1016/0022-2364(90)90104-H

Kleinberg, R. L., Kenyon, W., & Mitra, P. (1994). Mechanism of NMR Relaxation of Fluids in Rock. *Journal of Magnetic Resonance*, *108*, 206–214. http://www.sciencedirect.com/science/article/pii/S1064185884711120

Korringa, J., Seevers, D. O., & Torrey, H. C. (1962). Theory of spin pumping and relaxation in systems with low concentration of electron spin resonance centers. *Physical Review*, *127*(4), 1143–1150.

Krohn, C. E. (1988). Sandstone fractal and Euclidean pore volume distributions. *Journal of Geophysical Research*, 93(B4), 3286-3296. doi:10.1029/JB093iB04p03286.

Lindquist, W. B., Lee S. M., Coker, D., Jones, K., & Spanne, P. (1996). Medial axis analysis of void structure in three-dimensional tomographic images of porous media. *Journal of Geophysical Research*. *101*(B4), 2156-2202.

Lindquist, W.B., & Prodanovic, M. (2004, June 13-17) *3DMA-Rock - a software package for automated analysis of rock pore structure in 3-D computed microtomography images*. Paper presented at Computational Methods in Water Resources XV Conference.

Lindquist, W.B., Venkatarangan, A., Dunsmuir, J., & Wong, T. (1999). Pore and throat size distributions measured from sychrotron X-ray tomographic images of Fontainebleau sandstones. *Journal of Geophysics Research, 105*(B9), 2156-2202. ftp://ftp.ams.sunysb.edu/pub/papers/1999/susb99_13.pdf

Markley, J. L., Horsley, W. J., & Klein, M. P. (1971). Spin-Lattice Relaxation Measurements in Slowly Relaxing Complex Spectra. *The Journal of Chemical Physics*, *55*(7), 3604. http://doi.org/10.1063/1.1676626

Marschall, D., Gardner J. S., Mardon, D., & Coates, G. R. (1995). *Method for correlating NMR relaxometry and mercury injection data*. Presented at the SCA Symposium Society of Core Analysis.

McDonald, G. G., & Leigh, J. S. (1973). A new method for measuring longitudinal relaxation times. *Journal of Magnetic Resonance*. *9*(3), 358–362. http://doi.org/10.1016/0022-2364(73)90177-7

Meiboom, S., & Gill, D. (1958). Modified spin-echo method for measuring nuclear relaxation times. *Review of Scientific Instruments*, *29*(8), 688–691. http://doi.org/10.1063/1.1716296

Nave, R. (2014). Continuous wave NMR [Online image]. Retrieved August 6, 2015 from http://hyperphysics.phy-astr.gsu.edu/Hbase/nuclear/nmrvar.html

Neuman, C. H. (1974). Spin echo of spins diffusing in a bounded medium. *The Journal of Chemical Physics*, 60(11), 4508. http://doi.org/10.1063/1.1680931

Padhy, G. S., Lemaire, C., Amirtharaj, E. S., & Ioannidis, M. A. (2007). Pore size distribution in multiscale porous media as revealed by DDIF-NMR, mercury porosimetry and statistical image analysis. *Colloids and Surfaces A: Physicochemical and Engineering Aspects*, 300(1-2 SPEC. ISS.), 222–234. http://doi.org/10.1016/j.colsurfa.2006.12.039

Peemoeller, H., Shenoy, R. ., & Pintar, M. (1981). Two-dimensional NMR time evolution correlation spectroscopy in wet lysozyme. *Journal of Magnetic Resonance*, *45*(2), 193–204. http://doi.org/10.1016/0022-2364(81)90116-5

Putte, K. (1970). Elimination of Hl inhomogeneity and spin-spin relaxation in the determination of spin-lattice relaxation times. *Journal of Magnetic Resonance*. *2*(2), 174-180. http://dx.doi.org/10.1016/0022-2364(70)90068-5

Ramsey, N. F. (1950). Magnetic shielding of nuclei in molecules. *Physical Review*, *78*(6), 699–703. http://doi.org/10.1103/PhysRev.78.699

Sezginer, A., Kleinberg, R. L., & Fukuhara, M. (1991). Very rapid simultaneous measurement of nuclear magnetic resonance spin-lattice relaxation time and spin-spin relaxation time. *Journal of Magnetic Resonance*. *527*, 504–527.

C. P. Slichter. (1978). *Principles of Magnetic Resonance* (2nd edition). Berlin: Springer-Vcrlag.

Straley, C., Morriss, C. E., Kenyon W.E., & Howard, J. J. (1991, June 16-19). *NMR in partially-saturated rocks: laboratory insights on free fluid index and comparison with borehole logs*. Paper presented at the SPWLA Thrity-Second Annual Logging Symposium.

Young, Thomas. (1805). An essay on the cohesion of fluids. *Philosophical Transactions of the Royal Society of London*, *95,* 65–87.